Vacuum 221 (2024) 112926

Contents lists available at ScienceDirect

Vacuum

journal homepage: www.elsevier.com/locate/vacuum

DFT aided prediction of phase stability, optoelectronic and thermoelectric properties of A_2AuScX_6 (A= Cs, Rb; X= Cl, Br, I) double perovskites for energy harvesting technology

S. Mahmud [a,b], M.A. Ali [a,*], M.M. Hossain [a], M.M. Uddin [a]

[a] Advanced Computational Materials Research Laboratory, Department of Physics, Chittagong University of Engineering and Technology (CUET), Chattogram, 4349, Bangladesh

[b] Department of Electrical and Electronic Engineering, Jatiya Kabi Kazi Nazrul Islam University (JKKNIU), Mymensingh, 2224, Bangladesh

ARTICLE INFO

Handling editor: Per Eklund

Keywords:
Double perovskite halides
DFT computation
Phase stability
Optoelectronic properties
Thermo-electric properties
Thermo-mechanical properties

ABSTRACT

In this work, the density functional theory (DFT) was used to predict the physical properties of A_2AuScX_6 (A = Cs, Rb; X = Cl, Br, I) double perovskites (DPs). The stability was confirmed by computing the formation energy, binding energy, phonon dispersion curve, stiffness constants, tolerance, and octahedral factors. The nature of electronic conductivity and chemical bonding were explored. The band gap values using TB-mBJ are 1.88, 1.68, and 1.30 eV for Cs_2AuScX_6 [X = Cl, Br, I] and 1.93, 1.71, and 1.32 eV for Rb_2AuScX_6 [X = Cl, Br, I], respectively. The dielectric function, absorption coefficient, refractive index, energy loss function, photoconductivity, and reflectivity were also calculated and analyzed. The absorption coefficients in the visible range are 0.333×10^6 cm^{-1}, 0.27×10^6 cm^{-1}, and 0.213×10^6 cm^{-1} for Cs_2AuScX_6 [X = Cl, Br, I] and 0.345×10^6 cm^{-1}, 0.281×10^6 cm^{-1}, and 0.218×10^6 cm^{-1} for Rb_2AuScX_6 [X = Cl, Br, I], respectively. We also investigated the thermoelectric properties and found the figure of merit (ZT) values of 0.44, 0.47, and 0.62 for Cs_2AuScX_6 (X = Cl, Br, I) and 0.47, 0.53, and 0.54 for Rb_2AuScX_6 (X = Cl, Br, I) at 300 K. The results revealed that the studied compounds are potential candidates for solar cells and thermoelectric devices.

1. Introduction

The demand for energy has rapidly increased in recent years. As a result, experts are diligently searching for alternative energy sources in addition to traditional fossil fuels. Solar radiation, a massive energy source, can be used effectively to generate power [1]. As a result, scientists are working hard to explore materials that are inexpensive, reliable, and proficient in using solar radiation to harvest energy. The photovoltaic process offers a reliable way to generate renewable energy [2].

Perovskites are semiconducting materials that can carry electric charges when exposed to light. The chemical formula for the perovskite crystal structure is ABX_3, where A and B are cations and X is an anion. A type of substance known as "double perovskite" has a perovskite crystal structure, but two distinct cations occupy the B-site of the structure. A double perovskite has the formula $A_2BB'X_6$ because the B-site contains two distinct cations. The B and B′ cations may alter, but the A-site cation stays the same as in a typical perovskite. This configuration offers various features and capabilities and permits different cation combinations. The double perovskite (DP) structure of A_2AuScX_6 ($A = Cs^+/Rb^+$; $X = Cl^-/Br^-/I^-$) consists of two interpenetrating face-centered cubic lattices, one formed by Cs^+/Rb^+ cations and the other by Au^{1+}, Sc^{3+}, and X^- anions. The choice of Au and Sc as the transition metal cations in each substance is particularly significant. Au is a noble metal known for its excellent electrical conductivity, while Sc is recognized for its tunable bandgap and favorable optoelectronic properties. Combining these two elements in the B-site of the double perovskite halide makes it possible to tailor the material's electronic band structure and charge transport properties. This tenability is essential for optimizing the material's performance in electronic and optoelectronic devices. The halide component, X (chloride, bromide, or iodide), plays a crucial role in determining the overall properties, especially influencing the electronic band structure and affecting the material's absorption characteristics. Also, by controlling the halide composition, researchers can modulate the energy levels and light absorption properties of materials, further enhancing their potential for optoelectronic applications. It is important

* Corresponding author.
E-mail address: ashrafphy31@cuet.ac.bd (M.A. Ali).

https://doi.org/10.1016/j.vacuum.2023.112926
Received 4 November 2023; Received in revised form 3 December 2023; Accepted 19 December 2023
Available online 23 December 2023

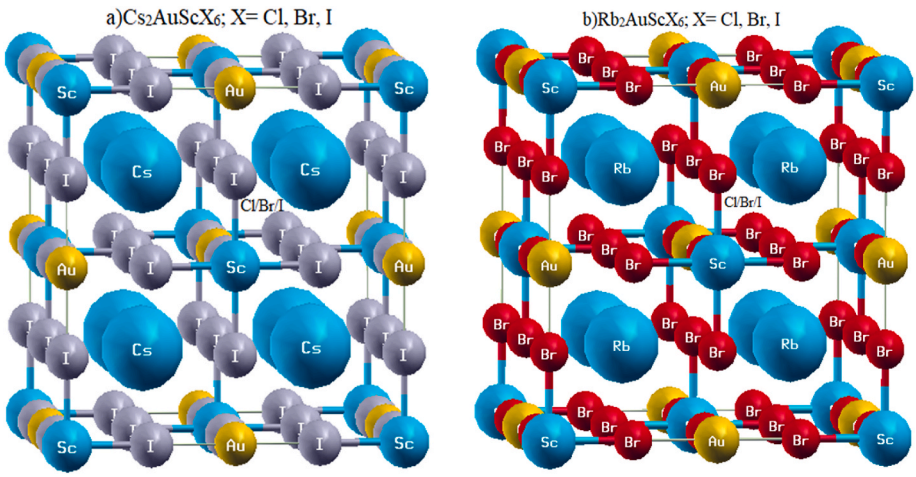

Fig. 1. Unit cell of a) Cs_2AuScX_6 and b) Rb_2AuScX_6; (X = Cl, Br, I).

to remember that DP can support B-site elements with oxidation states ranging from 1^+ to 4^+, whereas ABX_3 can only handle 2^+ B-site cations [3]. Moreover, the zero oxidation state, a charge balance typical of perovskite halides, may be recognized by combining tetravalent ions with a vacancy at BB'. Moreover, the band gap would be direct or indirect, with larger values, which is impractical for solar cell use.

The organic-inorganic mixed or hybrid halide perovskite $CH_3NH_3PbX_3$ ($MAPbX_3$; X = Cl/Br) has received a lot of interest as a key component in the fabrication of extremely effective solar cells due to its excellent efficiency [4–9]. Scientists have put in a lot of work to increase efficiency from 3.8 % in 2009 to 26.08 % in 2023 [10–14]. The strong absorbance of light in the visible area and outstanding stability of organic-inorganic mixed or hybrid halide perovskite lead to their superior performance [15,16]. However, lead (Pb), which cannot be commercialized on a big scale due to its poor stability and toxicity, necessitates the search for other materials as alternatives for B-sites.

Recently, there has been a lot of excitement in double perovskite (DP) halides due to their potential applications in various fields, including opto-electronics [17–19], magnetism [20–22], catalysis [23–25], and energy conversion [5,26–28]. They also have a range of exciting properties that make them potential for next-generation electronic devices and energy technologies, including magneto-resistance [29], multi-ferroicity [30], and high spin-orbit coupling [31]. The DP halide group introduces a new opportunity for photovoltaic and optoelectronic devices. However, determining the most suitable one with the best optoelectronic properties is challenging. Additionally, DP has gained importance in optoelectronic studies [32,33] because of its capacity to accept a variety of metal cations. Scientists are now conducting research on the DPs to develop new materials with enhanced functionality, which will, in turn, help them better understand the structure-property correlations associated with these materials. These materials offer great promise for enhancing technology across various sectors, potentially leading to more efficient and eco-friendly devices. For example, Slavney et al. [32] prepared and examined $Cs_2AgBiBr_6$ double perovskite, which is an interesting choice for optical and solar applications. Mcclure [34] experimentally synthesized the Cs_2AgBiX_6 (X = Cl/Br) solid solution and found an indirect band gap of 2.77 and 2.19 eV that are somewhat less than the band gaps of the similar lead halide perovskites, 3.00 eV for $CH_3NH_3PbCl_3$ and 2.26 eV for $CH_3NH_3PbBr_3$. F. Igbari et al. [35] effectively prepared $Cs_2AgBiBr_6$ with an energy gap measured at 1.95 eV, suggesting it as a potential photovoltaic material. A DP of $Cs_2AgInCl_6$ with high photosensitivity characteristics and a direct band nature was created by Volonakis et al. [36]. In addition, many researchers have used the DFT approach for double-halide perovskite in solar cells since it is a cost-effective and time-efficient alternative. Dhar et al. studied the lead-free DP halide of the Cs_2ScInX_6 (X = Cl/Br) compound theoretically and found a direct band gap of 0.637 and 0.81 eV for an optoelectronic device [3,37]. N.E. et al. showed the optoelectronic and thermal properties of Cs_2ScTlX_6 (X = Cl/Br/I) for renewable energy applications with band gap of 3.85 eV (direct), 3.2 eV (direct), and 2.75 eV (indirect). But these compounds exhibited better thermo-electric properties (figure of merit 0.61 to 0.66) compared to Cs-based halide [38]. Yanming Sun et al. and Pan Liu et al. integrated first-principles DFT calculations with experimental studies to demonstrate the stability mechanism and Mn^{2+}-driven luminous feature for the advancement of DP halides of $Cs_2LiBiCl_6$ [39] and Cs_2KBiCl_6 [40], respectively. Recently, Ashiq et al. developed B-site cations of Sc and Au-based K_2ScAuZ_6 (Z = Br/I) DP halides for harvesting energy appliances with the indirect band gap values of 2.00 and 1.45 eV and ZT values of 0.80 and 1.00 at 200 K without considering the lattice part [41].

We selected a group of double halide compounds of A_2AuScX_6 (A = Cs, Rb; X = Cl, Br, I). Six halides are present here: the alkaline metal Cs/Rb (group 1) and the rare earth soft metal Sc (group 3) are both paramagnetic, while the metal Au (group 11) is diamagnetic. To our knowledge, the aforementioned materials have not been the subject of any theoretical or applied research. The prediction of some new materials with better optoelectronic properties suitable for energy technologies is the primary goal of the present research.

Thus, the structural stability, optoelectronic properties, and thermoelectric properties of the herein predicted A_2AuScX_6 halides (where A = Cs, Rb, and X = Cl, Br, and I) have been studied in this work. We anticipate that our study will offer vital guidance for predicting lead-free DP materials that may be used in future thermoelectric devices and solar cells. In addition, as a routine check, this article also discussed the thermo-mechanical characteristics of the studied materials.

2. Computational technique

This task was carried out by the Wien2k code [42] using the DFT on the Kohn-Shams equation. For this, firstly, ground state variables are computed using the Generalized Gradient Approximation (GGA) Perdew-Burke-Ernzerhof (PBE) [43] approach with the FP-LAPW (full potential linearized augmented plane wave) [44] method for structural optimization by establishing the Birch-Murnaghan 3rd state of the equation. Initialization was performed using the following parameters: bond length factor of 3, energy required for valence and core state separation of −6.0 Ry, R-MT*K-MAX of 7, number of employed k-points of 1000 (10 × 10 × 10), and GMAX of 12. The DFT calculation in Wien2k involves SCF (self-consistent field), which solves the Kohn-Shams equation by updating the charge density on the electronic wave function. When calculating SCF, the energy convergence (ec) and charge

Table 1
Optimized lattice parameter, volume, and structural entity with Fm-3m space group (#225) in non-polarized (NP) states of A_2AuScX_6 (A = Cs, Rb; X = Cl, Br, I).

Parameter	$Cs_2AuScCl_6$	$Cs_2AuScBr_6$	Cs_2AuScI_6	$Rb_2AuScCl_6$	$Rb_2AuScBr_6$	Rb_2AuScI_6
$a = b = c$ (Å)	10.5326	11.0869	11.8920	10.4480	11.0197	11.8452
$a = b = c$ (Bohr)	19.9037	20.9513	22.4726	19.7438	20.8243	22.3841
V (Bohr^3)	1989	2290	2835	1924	2257	2788
t_G	0.90	0.89	0.87	0.87	0.86	0.85
μ	0.58	0.53	0.48	0.58	0.53	0.48
E_F (eV/atom)	−2.38	−2.00	−1.56	−2.34	−1.95	−1.50
E_b (eV/atom)	−4.03	−3.65	−3.25	−4.01	−3.63	−3.22
E_0 (Ry)	−76324.63	−102066.17	−156214.92	−57089.40	−82830.94	−136979.68
B_0	34.38	32.38	23.20	34.87	30.75	24.52
$B_0^{'}$	6.03	5.52	4.42	5.39	4.40	3.74

convergence (cc) criteria are set at 0.0001Ry and 0.001e, respectively. Thermal and mechanical investigations are also conducted using the IR-Elast program [45]. In order to deliver more accurate results, we used the Trans Blaha modified Becke-Johnson (TB-mBJ) [46] methodology for optoelectronic characteristics since it maintains a balance between precision and computing time for inorganic compounds. The Boltztrap2 algorithm [47] was used to determine the behavior of thermal electronic transport, with the exception of lattice vibration. The 1 × 1 × 1 supercell concept was used to perform the calculation of phonons using the technique of finite displacement. For this computation, we used the following electron-valence configurations: $5p^6 6s^1$ for the Cs, $4p^6 5s^1$ for the Rb, $5d^{10} 6s^1$ for the Au, $4s^2 3\,d^1$ for the Sc, $3s^2 3p^5$ for the Cl, $4s^2 4p^5$ for the Br, and $5s^2 5p^5$ for the I.

3. Results and discussion

3.1. Structural properties and stability

Fig. 1 depicts the cubic crystal structure of A_2AuScX_6 (A = Cs, Rb; X = Cl, Br, I) double perovskite (DP) halides, where the four formula units are present in the ratio of 2:1:1:6 and are comparable to the basic perovskite of ABX_3. The DP structures are made up of 8 Cs/R_b atoms, 13 [Au-X_6] octahedral, and 14 [Sc-X_6] octahedra. These are all members of the face-centered Fm-3m (225) symmorphic space group and are located in the Wyckoff positions such as 8c, 4a, 4b, and 24e of the corresponding atoms Cs/R_b (0.25, 0.25, 0.25), Au (0.5, 0.5, 0.5), Sc (0, 0, 0), and Cl/Br/I (0.25, 0, 0).

In this work, the lattice constant increases consistently as the halide atom transitions from Cl to Br to I. The crystal structure was optimized using the GGA-PBE function. Table 1 displays the estimated lattice parameter with the lowest energy at the optimum volume.

The DP structural materials for a cubic system's stability are determined by the tolerance factor (t_G) and octahedral factor (μ), which were established by Goldsmith [48], and the following equations are given below:

$$t_G = \frac{R_A + R_X}{\sqrt{2}\left(\frac{R_{B^{'}} + R_{B^{''}}}{2} + R_X\right)}$$

$$\mu = \frac{R_{B^{'}} + R_{B^{''}}}{2R_X}$$

where R represents the efficient ionic radii of each element in the above expressions. So that $R_A = 1.88$ and 1.72 for Cs^+ and R_b^+, $R_{B^{'}} = 1.37$ for Au^+, $R_{B^{''}} = 0.745$ for Sc^{3+}, and $R_X = 1.81$, 1.96, and 2.2 for Cl^-, Br^-, and I^-, which were taken by the Shannon ionic radius [49]. Table 1 presents the obtained tolerance and octahedral factors of the titled materials, and these results witness stable structures within the range of 0.81–1.1 and 0.41 to 0.89 [50], respectively.

Furthermore, the formation energy and binding energy serve as further confirmation for the dynamic stability of the DP halides of A_2AuScX_6, which is calculated by the following equations [51]:

$$E_f = \frac{E_{A_2AuScX_6} - n_A \times \frac{E_A}{k} - n_{Au} \times \frac{E_{Au}}{l} - n_{Sc} \times \frac{E_{Sc}}{m} - n_X \times \frac{E_X}{p}}{N}$$

$$E_b = E_{A_2AuScX_6} - n_A \times \mu_A - n_{Au} \times \mu_{Au} - n_{Sc} \times \mu_{Sc} - n_X \times \mu_X$$

where, $E_{A_2AuScX_6}$ denotes the total energy of A_2AuScX_6. E_A, E_{Au}, E_{Sc}, E_X and n_A, n_{Au}, n_{Sc} and n_X denotes the energy and number of atoms of Cs/Rb, Au, Sc, and Cl/Br/I, respectively. The coefficients k, l, m, and p are the number of individual atoms per unit cell, and N is the total number of atoms in compounds. The μ represents the individual Free State energy of the total atom. The negative sign of formation energy confirmed their stability; higher negativity shows greater stability. Consequently, $A_2AuScCl_6$ is more stable than $A_2AuScBr_6$ and A_2AuScI_6 for the respective Cs and Rb-based halides.

To evaluate the mentioned compound's thermodynamic stability, we computed its decomposition energy by considering potential pathways. For this purpose, we use the experimentally identified stable phases of $CsAuCl_3$ [52], $CsAuBr_3$ [53], $CsAuI_3$ [54], CsI [55], RbI [56], ScI_3 [57], Au [57], and the proto-type of $Cs_3Cr_2Cl_9$ [58] for Cl and Br-based compounds. The potential decomposition routes from OQMD for three halides based on Cs and Rb are outlined below [57]:

$$Cs_2AuScCl_6 = \frac{1}{4}\,CsAuCl_3 + \frac{7}{10}Cs_3Sc_2Cl_9 + \frac{1}{20}Au$$

$$Cs_2AuScBr_6 = \frac{1}{4}\,CsAuBr_3 + \frac{7}{10}Cs_3Sc_2Br_9 + \frac{1}{20}Au$$

$$Cs_2AuScI_6 = \frac{1}{4}\,CsAuI_3 + \frac{3}{10}CsI + \frac{2}{5}ScI_3 + \frac{1}{20}Au$$

$$Rb_2AuScCl_6 = \frac{1}{4}\,RbAuCl_3 + \frac{7}{10}Rb_3Sc_2Cl_9 + \frac{1}{20}Au$$

$$Rb_2AuScBr_6 = \frac{1}{4}\,RbAuBr_3 + \frac{7}{10}Rb_3Sc_2Br_9 + \frac{1}{20}Au$$

$$Rb_2AuScI_6 = \frac{1}{4}\,RbAuI_3 + \frac{3}{10}RbI + \frac{2}{5}ScI_3 + \frac{1}{20}Au$$

The decomposition enthalpies calculated for $Cs_2AuScCl_6$, $Cs_2AuScBr_6$, and Cs_2AuScI_6 are 23, 18, and 10 meV/atom, while for $Rb_2AuScCl_6$, $Rb_2AuScBr_6$ and Rb_2AuScI_6, they are 19, 15, and 8 meV/atom, respectively. The positive decomposition enthalpy values demonstrate these compounds thermodynamic stability, showing that the energy is derived from the compound's decomposing phases. The third-order Birch-Murnaghan equation of state [59], which supports cubic stability with non-magnetic characteristics and lowest energies, is used in the present samples to optimize the structural or energy volume of the named DPs. A solid's volume and the pressure it experiences are related by the Birch-Murnaghan 3rd-order equation of state, which is given below-

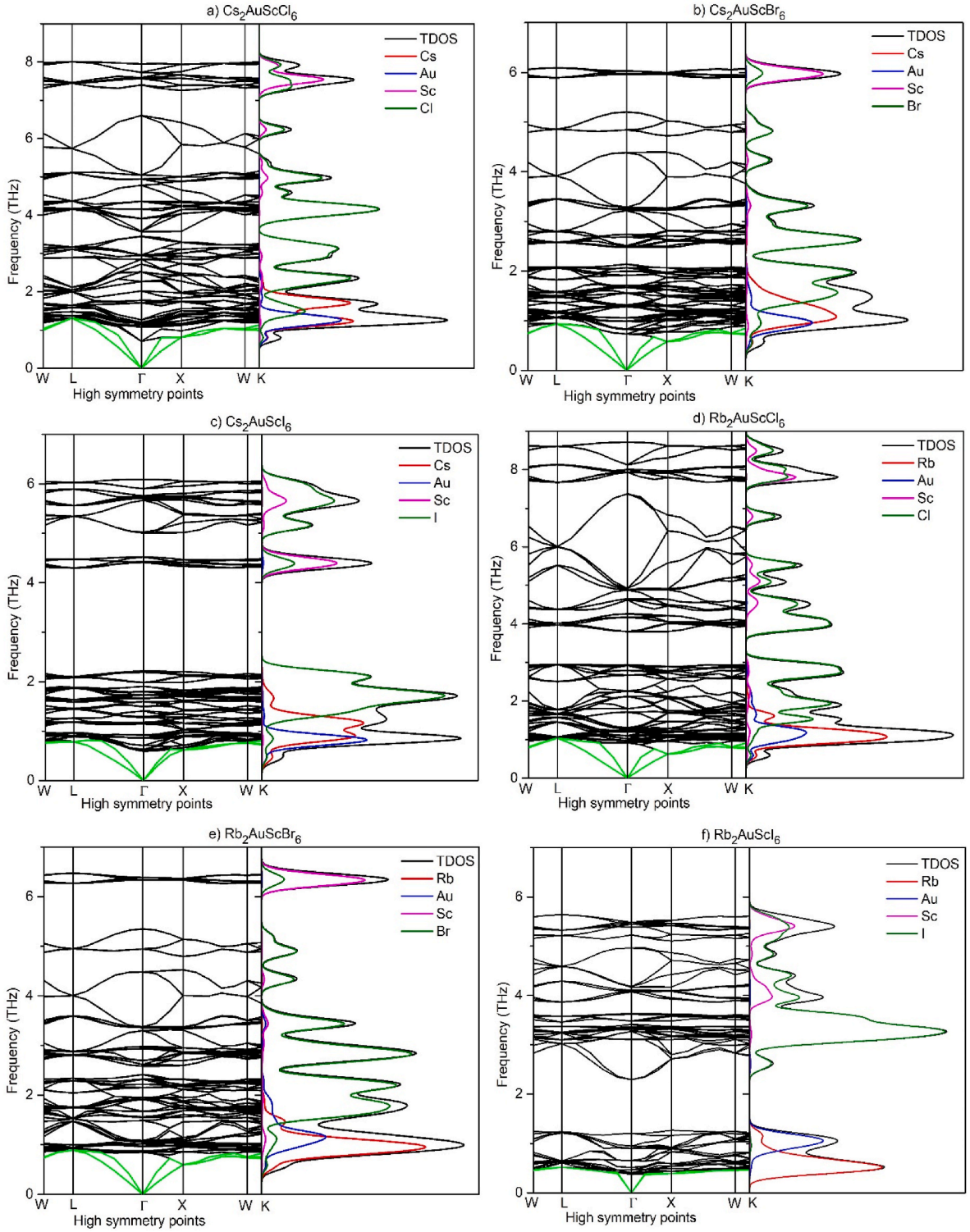

Fig. 2. Phonon dispersion curves with phonon DOS of a) $Cs_2AuScCl_6$, b) $Cs_2AuScBr_6$, c) Cs_2AuScI_6, d) $Rb_2AuScCl_6$, e) $Rb_2AuScBr_6$, f) Rb_2AuScI_6.

$$E(V) = E_0 + \frac{9V_0B_0}{16} + \left[\left\{\left(\frac{V_0}{V}\right)^{2/3} - 1\right\}^3 B_0' + \left\{\left(\frac{V_0}{V}\right)^{2/3} - 1\right\}^2 - \left\{6 - 4\left(\frac{V_0}{V}\right)^{2/3}\right\}\right]$$

where E(V) stands for the internal energy of the material, E_0 stands for minimum or ground state energy, V_0 stands for the reference or standard volume, V stands for the volume under stress, B_0 stands for zero pressure bulk modulus, and B_0' stands for pressure modified bulk modulus. These substances have positive B_0' values, indicating that they become stiffer when subjected to higher pressure. The ground-state energy's negative value also represents the stability and growth of that stability for denser materials. The energy vs volume curve of the materials under investigation is shown by supplementary information (see Fig. 1S). We have also determined the lattice constant (a) of all compounds from the E-V fitting curve. The atomic radius increases the lattice parameter in

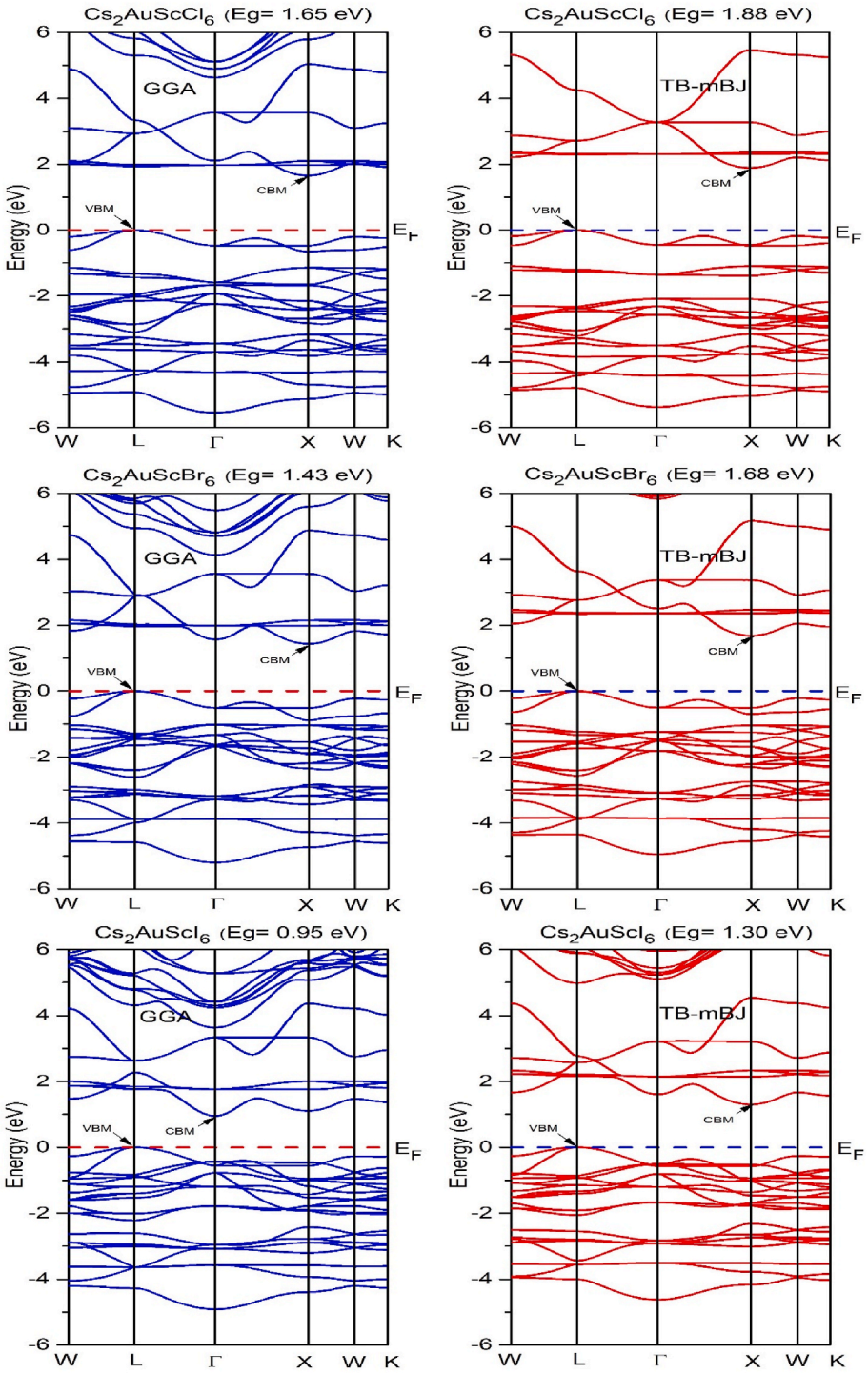

Fig. 3. Energy band diagram of Cs-based halide of $Cs_2AuScCl_6$, $Cs_2AuScBr_6$, Cs_2AuScI_6 computed by GGA-PBE (Left side) and TB-mBJ (Right side) approach.

compositions based on Cl, Br, and I, and these shifts demonstrate the validity and accuracy of the study.

The phonon dispersion curve (PDC) of A_2AuScX_6 (A = Cs, Rb; X = Cl, Br, I) with PDOS is depicted in Fig. 2. The dynamic stability of all compounds under investigation is demonstrated by the absence of imaginary frequency throughout the whole Brillion Zone (BZ). With 10 atoms, these unit cell compositions must have 3 N, or 30 vibrational modes, of which three are acoustic and operate in the low-frequency region (less than 1 THz), and the remaining 27 are optic and operate in the high-frequency range (greater than 1 THz). These are known as zero-point frequency and non-zero-point frequency, respectively. All compounds' phonon particles are stable along the following routes: W to L, L to Γ, Γ to X, X to W, and W to K. The compound's phonon DOS (PDOS) is displayed next to the dispersion curve for better understanding. We observed a strong peak in PDOS for flat bands and a negligible peak for non-flat bands. Both the phonon DOS and the frequency dispersion are precisely adjusted. It is shown that the low-frequency (below 2 THz) lattice vibrations coincide with the optic modes and are mainly ascribed to contributions from Cs/Rb and Au atoms.

In contrast, the halide ions (for Cl and Br) dominate the mid-level vibrations, whereas Sc ions work in tandem with Cl/Br ions to dominate the high-frequency area in Cs and Rb-based DPs. However, for

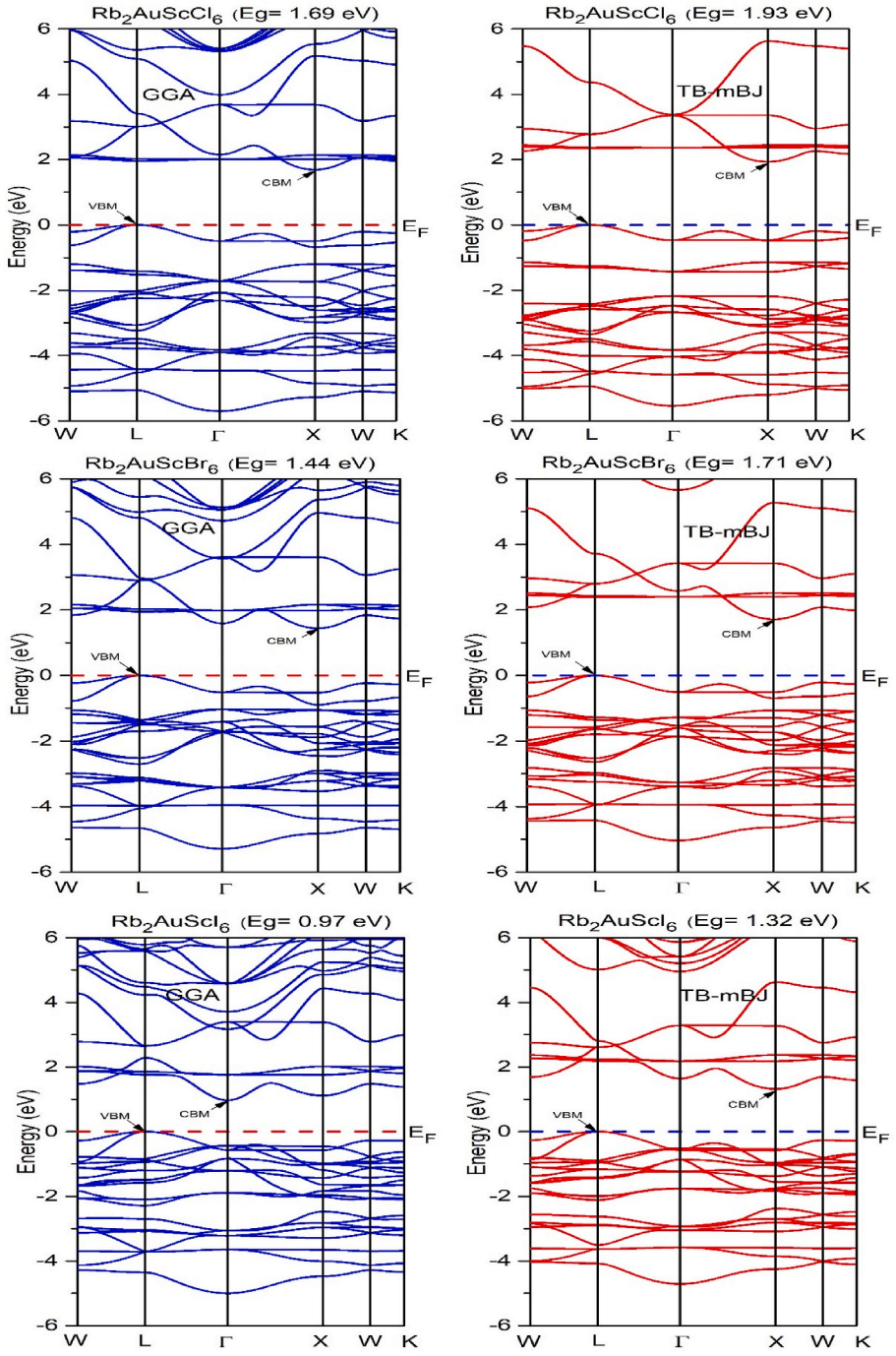

Fig. 4. Energy band diagram of Rb-based halide of $Rb_2AuScCl_6$, $Rb_2AuScBr_6$, and Rb_2AuScI_6 computed by GGA-PBE (Left side) and TB-mBJ (Right side) method.

Cs_2AuScI_6 and Rb_2AuScI_6, there is a phononic gap in the middle-frequency range, and I ions work in concert with Sc to generate high-frequency vibrations. As shown in the supplementary part (see Table S1), the poor lattice thermal conductivity of the investigated compounds was caused by the restriction of the phonon dispersion heat resulting from the overlap of acoustic and optical modes in the low-frequency ranges.

3.2. Electronic properties and the effective mass of charge carriers

The carrier transport channel may be seen visually through the features of conductors, semiconductors, and insulator's electronic characteristics. Further information about a material's intended applications may be gleaned from its electronic characteristics, such as its band structure and the distribution of electrons inside those bands (known as the total and partial density of states) [60]. The band gap values of A_2AuScX_6 (A = Cs, Rb; X = Cl, Br, I) are essential in deciding whether they are suitable for use in photovoltaic or thermoelectric applications or not. We used the TB-mBJ potential [61] to forecast the band gap with more accuracy. Every material has an empty Femi level, which indicates that it possesses a semiconducting nature. In addition, the materials are non-magnetic and show reductions (shifts) in the band structure at the Fermi level when Br or I replace Cl, the halide component.

The GGA-PBE functional technique was first used to investigate the electronic band structure. GGA-PBE + SOC was then employed to observe any SOC effect on the band structure. The band structure

Table 2
Computed band gaps for Cs-based halide of $Cs_2AuScCl_6$, $Cs_2AuScBr_6$, Cs_2AuScI_6, and Rb-based halide of $Rb_2AuScCl_6$, $Rb_2AuScBr_6$, and Rb_2AuScI_6.

Compound	GGA-PBE	TB-mBJ	Nature	Reference
$Cs_2AuScCl_6$	1.65	1.88	Indirect	This work
$Cs_2AuScBr_6$	1.43	1.68	Indirect	This work
Cs_2AuScI_6	0.95	1.30	Indirect	This work
$Rb_2AuScCl_6$	1.69	1.93	Indirect	This work
$Rb_2AuScBr_6$	1.44	1.71	Indirect	This work
Rb_2AuScI_6	0.97	1.32	Indirect	This work
$K_2AuScBr_6$	–	2.00	Indirect	[41]
K_2AuScI_6	–	1.45	Indirect	[41]

calculated using these functional methods revealed that the SOC impact on the studied compounds is very small (±0.04). The band structure of all materials under study is displayed in Figs. 3 and 4, utilizing the GGA-PBE (left side) and TB-mBJ (right side) approaches. Here, we present a comparative study of three methods for measuring the bandgap: the traditional SCF, the SCF with SOC, and the well-known TB-mBJ technique.

The energy band gaps calculated using the GGA-PBE (TB-mBJ) potential are 1.65 (1.88), 1.43 (1.68), 0.95 (1.30), 1.69 (1.93), 1.44 (1.71), and 0.97 (1.32) eV for $Cs_2AuScCl_6$, $Cs_2AuScBr_6$, Cs_2AuScI_6, $Rb_2AuScCl_6$, $Rb_2AuScBr_6$, and Rb_2AuScI_6, respectively. The fact that the band gap of such substances decreases as the X atoms change from Cl to Br to I. The bandgap of the titled materials and a few other similar materials using TB-mBJ are compared in Table 2, which further supports the validity of the computed results for the materials under investigation. Every compound shows the same pattern, and TB-mBJ corrects the GGA-PBE's inaccuracy. The high symmetric points of W (0.50, 0.25, 0.75), L (0.5, 0.5, 0.5), Γ (0, 0, 0), X (0.5, 0, 0), W (0.50, 0.25, 0.75), and K (0.375, 0.375, 0.75) were the destinations of the Brillion zone route. The top of the VB route and the bottom of the CB are more parabolic in shape in the GGA-PBE and TB-mBJ approaches. From Figs. 3 and 4, it is clear that the valence band maximum (VBM) and the conduction band minimum (CBM) occur at various symmetry points (L→X for all studied compounds by the TB-mBJ approach; L→Γ only for Cs_2AuScI_6 and Rb_2AuScI_6 by the GGA-PBE approach), indicating that all DPs are indirect band gap semiconductors. According to the Shockley-Queisser (S.Q.) limit, the ideal band gap for a single-junction solar cell functioning under typical solar radiation circumstances is about 1.4 eV for the highest theoretical efficiency. This range is related to maximum light conversion efficiency [62–64].

The optimal band gap of $Cs_2B'In_{0.75}Bi_{0.25}I_6$ (B' = Li, Na, and K) was obtained in the range of 0.90–1.60 eV by the doping process and exhibits better visible light performance compared to an un-doped material [65]. Also, the typical energy ranges of perovskite bands are from 0.8 to 2.2 eV, and materials for photoelectric conversion (PEC) will be able to use this energy extensively [66]. The obtained band gap values are close to both S.Q. limit as well as the values mentioned in ref. 65. Thus, the studied A_2AuScX_6 (A = Cs, Rb; X = Cl, Br, I) perovskites exhibits suitable band gap values for PEC, showing great promise for future applications as highly photosensitive materials.

The band gaps estimated from the electronic band structure are slightly less than those obtained from the absorption spectrum for indirect band gap semiconductors [67]. A recent report revealed a significant aspect of indirect band gap semiconductors for photocatalytic applications owing to their lower radiative recombination rate [68]. Additionally, flat bands inside the CB are observed, indicating the existence of the second phase and potentially explaining the emergence of superconductivity [62]. This suggests that DP is a viable alternative for advanced uses in ultra-powerful magnet technology. The bands still have a detectable range but get broader when Cl takes the place of the halide Br/I atom.

Solar cells commonly employ silicon (Si) and germanium (Ge) because of their availability, self-passivation, and indirect band gap.

Table 3
Estimated effective masses of holes (m_h^*) and electrons (m_e^*) at the lowest point of CB (L) and Highest point of VB (X or Γ) of respective materials of A_2AuScX_6 (A = Cs, Rb; X = Cl, Br, I).

Compound	Approach	m_h^*/m_0	m_e^*/m_0	m_h/m_e
$Cs_2AuScCl_6$	GGA-PBE	0.32, 0.62[a]	0.15, 0.47[a]	2.13
	TB-mBJ	0.33, 0.61[a]	0.18, 0.46[a]	1.83
$Cs_2AuScBr_6$	GGA-PBE	0.28	0.14	2.00
	TB-mBJ	0.28	0.15	1.86
Cs_2AuScI_6	GGA-PBE	0.25	0.063	3.96
	TB-mBJ	0.25	0.14	1.78
$Rb_2AuScCl_6$	GGA-PBE	0.31	0.15	2.06
	TB-mBJ	0.32	0.18	1.77
$Rb_2AuScBr_6$	GGA-PBE	0.27	0.13	2.07
	TB-mBJ	0.27	0.14	1.92
Rb_2AuScI_6	GGA-PBE	0.25	0.064	3.90
	TB-mBJ	0.25	0.13	1.92

[a] Reference [67] for $Cs_2AgAsCl_6$.

Both a photon and a phonon are needed for an indirect band gap semiconductor to go from the valence band (VB) to the conduction band (CB), causing changes in momentum and energy. Since the two variables are inversely related, an ideal characteristic of an efficient solar cell is that the minority carrier diffusion length is higher than the absorber depth of the material [69]. Despite lower light absorption in indirect semiconductors, they often have a longer recombination lifetime and a larger diffusion length, making them viable for efficient solar cells with a sufficiently thick absorbing layer.

In addition, indirect band gap semiconductors are mostly preferred in thin-film solar cells due to their weaker light absorption, enabling a broader photon energy range, including lower-energy solar photons [70–72]. Moreover, materials with an indirect band gap are more defect-tolerant and generate less heat, which is crucial for solar cell durability. In concentrator photovoltaic, this heat reduction is especially advantageous. Additionally, tandem solar cells combine multiple materials with different band gaps for increased efficiency and can leverage indirect band gap materials to optimize energy conversion across the solar spectrum [32,73,74].

The term "effective mass of charge carriers" describes the mass of electrons or holes in a double perovskite halide. Their effective mass is essential in determining how charge carriers behave and react to outside stimuli like an electric field. The effective mass of DP can vary depending on the specific material and its composition. It is influenced by the material's band structure, which, in turn, depends on the types of halides and other elements present in the perovskite structure.

We have calculated the effective mass of charge carriers (electrons or holes) in DP of A_2AuScX_6 (A = Cs, Rb; X = Cl, Br, I) at high symmetry points of VBM and CBM. The formula used to determine the effective mass and hole by using the E-K dispersion of the respective materials is as follows:

$$m^* = \frac{\hbar^2}{(d^2E/dK^2)}$$

where, $\hbar = 1.05 \times 10^{-34}$ J/s. From the E-K dispersion curve, we get the values of d^2E/dK^2 by using the curve fitting of the respective parabolic curve at any symmetry points. The computed effective mass values are presented in Table 3. It is obvious that the predicted effective mass values are far lower than those reported by others [67] for other DPs. The reduced effective mass is advantageous for transferring carriers, which is very beneficial for solar materials. Therefore, the DPs of A_2AuScX_6 are all highly perfect photovoltaic materials and have much promise for use in various solar applications. The ratio of the effective masses of holes to electrons (m_h/m_e) has a significant impact on carrier mobility, which is determined by the effective mass. In general, less mobility results from a larger effective mass. Thus, in a semiconductor, the ratio influences the relative mobility of electrons and holes.

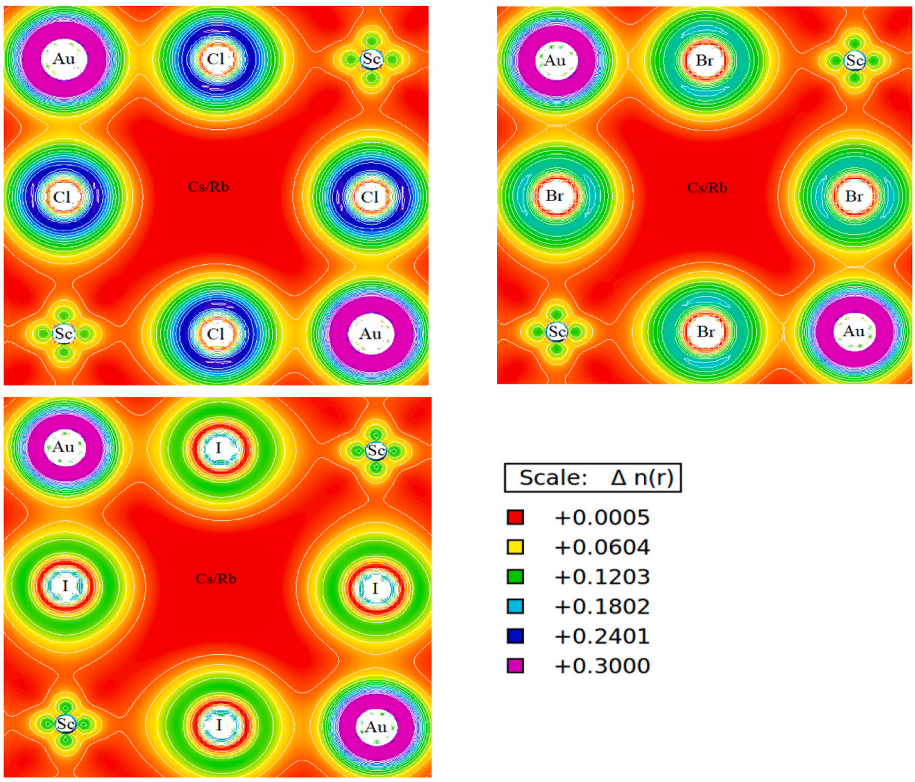

Fig. 5. Contour plot of charge density of a) $A_2AuScCl_6$, b) $A_2AuScBr_6$, and c) A_2AuScI_6; [A = Cs, Rb].

The titled compound's total and partial DOS and the key band structure characteristics found by the TB-mBJ potential are given in supplementary information (see Fig. 2S). It is clear that every DP compound has the same atomic state characteristics and ways of contributing. 0 eV was chosen as the Fermi level. Due to the little contribution of X-p orbitals, the Sc-d orbitals with hybridization (molecular orbital bonding) account for the majority of the CBM (conduction band minimum) of A_2AuScX_6. In DOS, the energy value of the band structure and the near E_F of CB match exactly. Au-*d* orbitals contribute the most to the VBM (valence band maximum), whereas X-*p* orbitals contribute the least. The band structure of PDOS and TDOS ultimately reflects the difference in energy levels between them. Rather than adding much to the band structure, the Cs^+/Rb^+ cation close to E_F mostly donates charges to preserve structural stability.

3.3. Nature of bonding

A_2AuScX_6 (A = Cs/Rb; X = Cl/Br/I) compounds belong to the DP family and have intriguing features because of their distinct bonding patterns and structures. It belongs to the class of inorganic DP, and the cations (Cs^+/Rb^+) and lattice have an impact on its characteristics. These materials' charge density and bonding type can be examined regarding their crystal structure and internal electronic interactions. The Space group Fm-3m characterizes the cubic crystal structure of the chemical mentioned.

The X ions (Cl, Br, or I) are positioned in the center of these octahedra in this structure, whereas the Au and Sc ions are situated in the corner, sharing octahedral positions. The spaces in between these octahedral Cs^+/Rb^+ ions are interstitial. This configuration creates a network of corner-sharing octahedra, which affects the compound's electronic and bonding characteristics. The charge density contour map for the materials in question is shown in Fig. 5.

The A ions (Cs/Rb) have relatively high electronegativity compared to Au and Sc, leading to ionic bonding between the A ions and the surrounding X ions. This results in forming A-X bonds with a certain degree of ionic character. The Au-Sc-X octahedral structure involves covalent bonding between the metal ions (Au and Sc) and the halogen ions (X). The electronegativity difference between the metal ions and X ions contributes to polar covalent bonds within the octahedral framework, similar to the reports published [67,75]. The metal-metal bonding (Au–Sc) within the octahedral can also have a metallic character due to the overlap of their atomic orbitals.

The combination of ionic, covalent, and metallic bonding interactions influences the charge density distribution in materials. The A ions contribute to the charge density by providing localized positive charge, while the X ions contribute localized negative charge due to electronegativity. In summary, the charge density and bonding nature of A_2AuScX_6 (A = Cs/Rb; X = Cl/Br/I) result from the complex interplay between ionic, covalent, and metallic bonding interactions within its crystal structure. This unusual bonding is the key to many of their desirable photovoltaic properties.

3.4. Optical properties

Optical characteristics reflect electronic properties and indicate how a material reacts to incident light. Photon energy in the region of 0–14 eV is used to study optical constants such as dielectric function, refraction index, absorption coefficient, and reflectivity for photoelectric/device applications of these DP materials.

The complex dielectric function may be represented by the real and imaginary components of the dielectric function with respect to photon energy, which is given by the following formula: $\epsilon(\omega) = \varepsilon_1(\omega) + i\varepsilon_2(\omega)$.

The real part of the dielectric constant $\varepsilon_1(\omega)$ indicates the amount of polarization when the external field is applied and can be calculated by the equations of Kramers-Kronig [76], while $\varepsilon_2(\omega)$ indicates an amount of electronic change or light absorption and can be calculated by the Kohn-Shams [77] equation, respectively.

$$\varepsilon_1(\omega) = 1 + \frac{2}{\pi} P \int_0^{\infty} \frac{\omega' * \varepsilon_2(\omega')}{\omega'^2 - \omega^2} d\omega$$

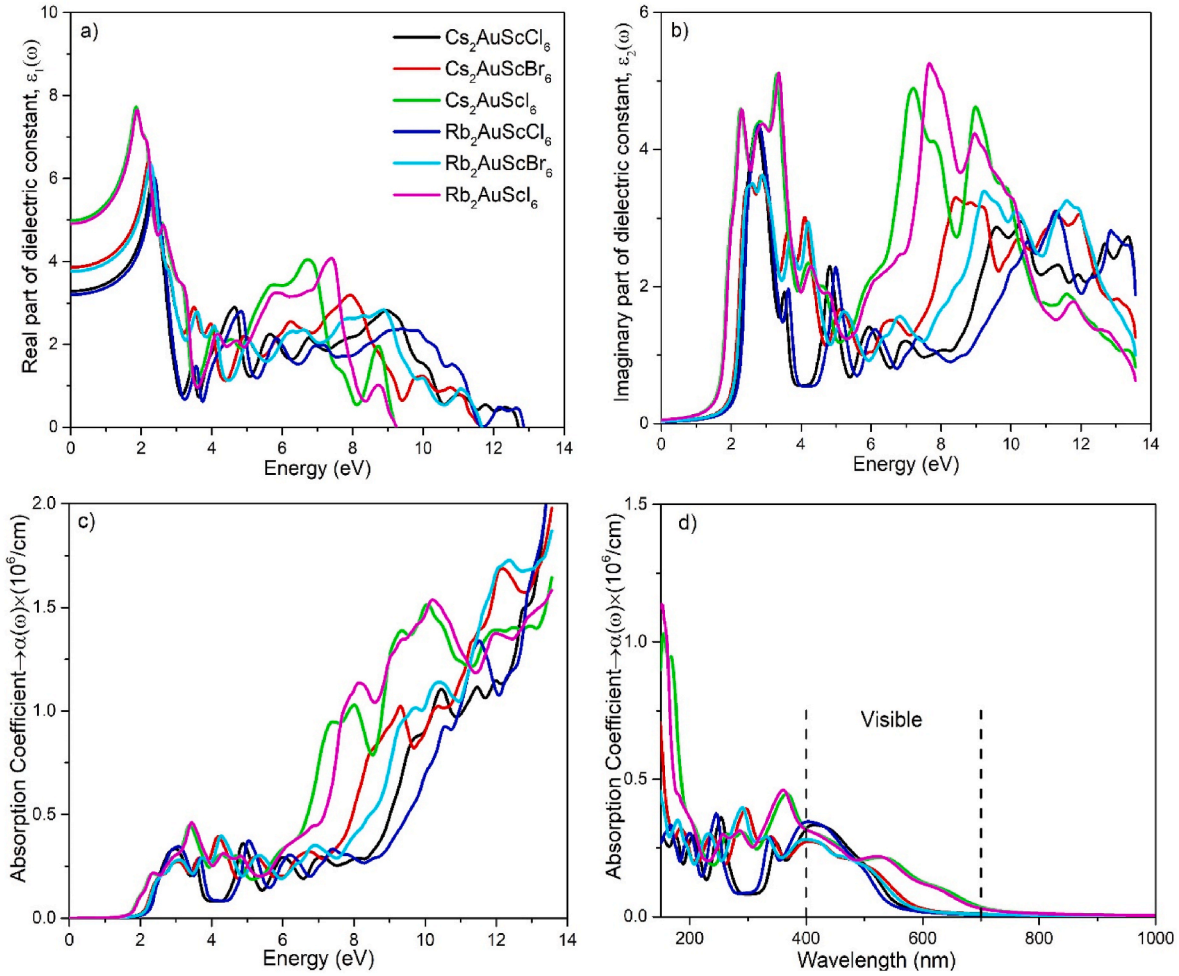

Fig. 6. Obtained values of a) real part of the dielectric constant, b) imaginary part of the dielectric constant, c) absorption coefficient in eV and d) absorption coefficient in nm for DP of $Cs_2AuScCl_6$, $Cs_2AuScBr_6$, Cs_2AuScI_6, $Rb_2AuScCl_6$, $Rb_2AuScBr_6$, and Rb_2AuScI_6.

$$\varepsilon_2(\omega) = \frac{Ve^2}{2\pi\hbar m^2\omega^2}\int d^3k\sum_{nn'}|(kn|p|kn')|^2 f(kn)\times\left(1-f(kn')\right)\delta(E_{kn}-E_{kn'}-\hbar\omega)$$

$$\varepsilon_1(0)\approx 1+\left[\frac{\hbar\omega_p}{E_g}\right]^2$$

where P in the first equation stands for the main component, the 2nd equation uses V, e, $\hbar$, p, kn, and kn' to represent unit volume, charge, decreasing plank constant, momentum transfer matrix, VB wave function, and CB wave function.

The dielectric function of the mentioned DP of A_2AuScX_6 is shown in Fig. 6(a and b). The real part of the dielectric constant $\varepsilon_1(\omega)$ first experienced a dramatic increase until it reached its maximum value, after which it began a downward trend. The static dielectric constants are 3.27 (3.19), 3.84 (3.76), and 4.97 (4.90) for A_2AuScX_6 [A = Cs, Rb; X = Cl, Br, I], and the highest value is seen to be 6.06 (6.03) at 2.33 (2.37) eV, 6.39 (6.36) at 2.22 (2.25) eV, and 7.70 (7.67) at 1.85 (1.89) eV for A_2AuScX_6 [A = Cs, Rb; X = Cl, Br, I], respectively. The Cs-based halides display slightly greater dielectric behaviour (static or dynamic) than the Rb-based halides. The minimal variation in $\varepsilon_1(\omega)$ for all compounds under study is, however, within −1.16 to −2 for energies greater than 10 eV, where the minus sign of $\varepsilon_1(\omega)$ indicates the compound's metallic character. Also, it was found that switching Cl with Br and I elevated the strength of the peaks of absorption and pushed them to a smaller energy region since I have a bigger electronic influence than Br and Cl. The static polarization and band gap are linked inversely by the Penn's model [78]:

where $\hbar$ and ω_p are the decreased plank constant and the frequency of the plasma, respectively.

The $\varepsilon_2(\omega)$ is significant because it determines the maximum absorption area and governs interband transitions that take place inside the materials used to fabricate devices. Due to the limitations of DFT, the transition points (VB to CB) exhibit a slight deviation from band structure and are plotted in Fig. 6(b). The maximum value of ε_2 is generally called the first absorption peak (FAP) and is responsible for the electronic transition at the Fermi level. In the case of $A_2AuScCl_6$ (A = Cs/Rb), the FAP is 2.71 and 2.79 eV, respectively. The remaining compounds have various peaks in the range of 4 eV, which were seen for $A_2AuScBr_6$ (A = Cs, Rb) at 2.54 (2.56) and 2.83 (2.88) eV and for A_2AuScI_6 (A = Cs/Rb) at 2.27 (2.30), 2.79 (2.88), and 3.29 (3.35) eV, respectively. For the titled compounds, we simply need to know the highest FAP values, which are 2.71, 2.54, and 2.27 eV for Cs_2AuScX_6 [X = Cl, Br, I] and 2.79, 2.56, and 2.30 eV for Rb_2AuScX_6 [X = Cl, Br, I], respectively. These values are in the visible range and indicate an effective absorption capacity. Compared to the DOS, the FAS originates mainly from the Au-d, along with the X-*p* at the VBM (valence band maximum) and the Sc-*d* at the CBM (conduction band minimum).

The absorption capacity $\alpha(\omega)$, is comparable to that of $\varepsilon_2(\omega)$, as illustrated by their coefficients at various energies (photon energy) and wavelengths, as shown in Fig. 6(c) and (d). The formula for the

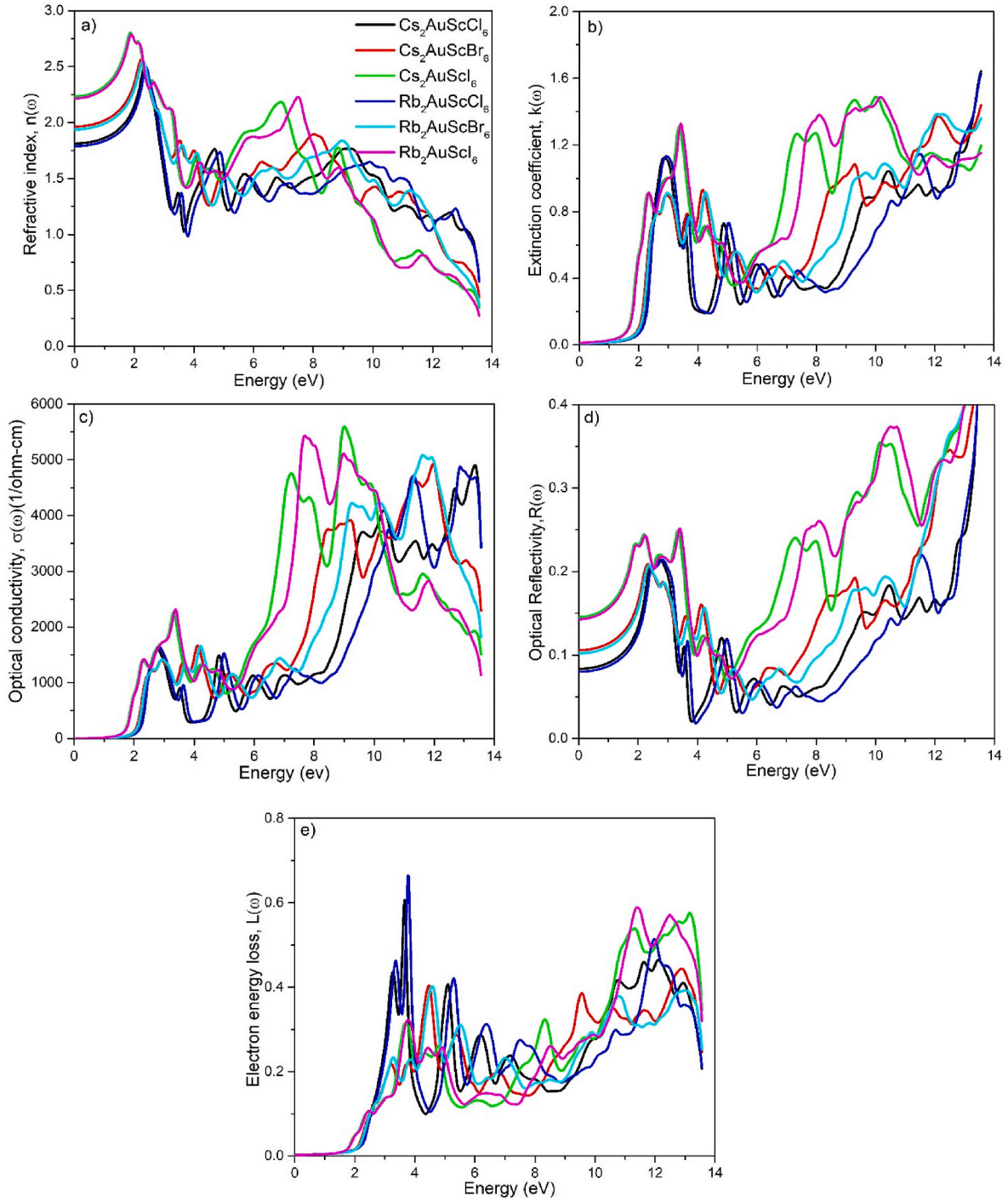

Fig. 7. The obtained a) refractive index, b) extinction coefficient, c) optical conductivity d) optical reflectivity, and e) electron energy loss of $Cs_2AuScCl_6$, $Cs_2AuScBr_6$, Cs_2AuScI_6, $Rb_2AuScCl_6$, $Rb_2AuScBr_6$, and Rb_2AuScI_6.

absorption coefficient α(ω) was derived from the imaginary and real parts of the dielectric function [74].

$$\alpha(\omega) = 2\omega\left(\frac{\left[\varepsilon_1^2(\omega)+\varepsilon_2^2(\omega)\right]^{1/2}-\varepsilon_1(\omega)}{2}\right)^{1/2}$$

The absorption edge, also known as the optical band gap or resultant value $\alpha(\omega)$ of the material, precisely corresponds to the electronic band gap, and the first highest absorption is observed at 2.95, 2.67, and 2.34 eV for Cs_2AuScX_6 [X = Cl, Br, I] and 3.07, 2.72, and 2.36 eV for Rb_2AuScX_6 [X = Cl, Br, I], respectively, which are in the visible range. Therefore, these DPs function well as absorbents for the visible spectrum. Other maximum absorption peaks, which also lie in the visible to UV range, are found at 3.03 (3.07) eV for $A_2AuScBr_6$ (A = Cs/Rb), and 3.11 (3.16) eV, and 3.36 (3.42) eV for A_2AuScI_6 (A = Cs/Rb). The development of several peaks with various peak intensities in the upper range from 7 to 13 eV illustrates the various possibilities of transitioning from filled to unfilled states. Besides, these materials have superior absorption coefficients than others DPs, such as 3 to 6.5 × 10^4 cm^{-1} for Cs_2CuBiX_6 (X = Cl/Br/I) [79], 4.8 to 5 × 10^4 cm^{-1} for Rb_2CuBiX_6 (X = Cl/Br) [80], 5 to 5.3 × 10^4 cm^{-1} for K_2CuBiX_6 (X = Cl/Br) [81], and 8 × 10^4 cm^{-1} for Cs_2AgBiI_6 [82], according to the highest peaks for all

compounds studied herein, which are situated at wavelengths of visible range (400–700 nm). The visible range absorption coefficients for $A_2AuScCl_6$ (A = Cs/Rb) are 0.333 (0.345) × 10^6 cm^{-1}. Other compounds show the different highest peaks in the visible to UV range; for instance, the peaks in $Cs_2AuScBr_6$ ($Rb_2AuScBr_6$) are 0.22 (0.224) × 10^6 cm^{-1} and 0.27 (0.281) × 10^6 cm^{-1}, and in Cs_2AuScI_6 (Rb_2AuScI_6) are 0.213 (0.218) × 10^6 cm^{-1}, 0.317 (0.32) × 10^6 cm^{-1}, and 0.446 (0.455) × 10^6 cm^{-1}, respectively. Due to their excellent photoelectric defining-features, these DP halide materials might be employed as the layer that absorbs sunlight in solar cells.

Other essential optical constants, such as the refractive factor n(ω), the extinction factor k(ω), the optical conductivity, the reflectivity R(ω), and the loss factor L(ω), are all calculated from the dielectric properties of all compounds [83–86].

$$n(\omega)=\left[\frac{\left\{\varepsilon_1^2(\omega)+\varepsilon_2^2(\omega)\right\}^{1/2}}{2}+\frac{\varepsilon_1(\omega)}{2}\right]^{1/2}$$

$$k(\omega)=\left[\frac{\left\{\varepsilon_1^2(\omega)+\varepsilon_2^2(\omega)\right\}^{1/2}}{2}-\frac{\varepsilon_1(\omega)}{2}\right]^{1/2}$$

$$\sigma(\omega)=\frac{\alpha nc}{4\pi}$$

$$R(\omega)=\frac{\{n(\omega)-1\}^2+k^2(\omega)}{\{n(\omega)+1\}^2+k^2(\omega)}$$

$$L(\omega)=\frac{\varepsilon_2}{\varepsilon_1^2+\varepsilon_2^2}$$

Fig. 7(a) displays the results of the refractive index calculation. The link between the real part of the dielectric function and the refractive index [$n^2(\omega)=\varepsilon_1(\omega)$], caused them to behave in the same way [87]. The static refractive factors of n(0) are 1.81 (1.79), 1.96 (1.93), and 2.22 (2.20), and their maximum values are 2.49 (2.48), 2.57 (2.53), and 2.80 (2.78), with 2.28 (2.37) eV, 2.20 (2.28) eV, and 1.84 (1.87) eV, for A_2AuScX_6; A = Cs/Rb, X = Cl/Br/I), respectively. Optoelectronic activities are appropriate for n(ω) values from 2.0 to 4.0 [88], and the studied materials have values within this range. The fact that the observed refractive factor values are greater than 1 is strong evidence for semiconducting materials. The refractive factor also evaluates the strength of the bonds—whether they are more or less than unity. A refractive index greater than one indicates the presence of covalent bonds rather than ionic ones. Due to photon slowing and increasing electron density, the aforementioned materials displayed covalent bonding, either static or dynamic [37].

The identical pattern of $\varepsilon_2(\omega)$ and $\alpha(\omega)$ is followed by the extinction factor k(ω), which detects the loss of electromagnetic (EM) waves in contents, as shown in Fig. 7(b). The connection between k(w) and α(ω) is as follows:

$$k=\frac{\alpha\lambda}{4\pi}$$

The value of the extinction coefficient was discovered to be extremely low, as would be predicted for semiconductor materials [89]. Any material's surface will absorb some of the incident light if a stream of photons at a specific frequency strikes it, initiating the interband transition or switching of electrons. The amount of real optical conductivity is used to measure this change. For optoelectronic devices to function practically, the optical conductivity, which is determined by the interband movement of electrons, must be within 1.4–4.0 eV in the visible range [88]. The initial peak exhibits maximum conductivities of 1594/1637 $(\Omega\text{-cm})^{-1}$ at 2.71/2.81 eV for $A_2AuScCl_6$ (A = Cs/Rb), 1227/1247 $(\Omega\text{-cm})^{-1}$ at 2.58/2.64 eV and 1401/1412 $(\Omega\text{-cm})^{-1}$ at 2.88/2.90 eV for $A_2AuScBr_6$ (A = Cs/Rb), and 1402/1417 $(\Omega\text{-cm})^{-1}$ at 2.29/2.31 eV, 1749/1755 $(\Omega\text{-cm})^{-1}$ at 2.99/3.01 eV and 2266/2299 $(\Omega\text{-cm})^{-1}$ at 3.29/3.35 eV for A_2AuScI_6 (A = Cs/Rb), respectively, while the highest value observed (4100–5500 1/Ω-cm) from 7 to 13 eV, as shown in Fig. 7(c).

Table 4
Computed optical constants.

Compound	$\varepsilon_1(0)$	n(0)	R(0)
$Cs_2AuScCl_6$	3.27	1.81	8.37 %
$Cs_2AuScBr_6$	3.84	1.96	10.70 %
Cs_2AuScI_6	4.97	2.22	14.58 %
$Rb_2AuScCl_6$	3.19	1.79	7.96 %
$Rb_2AuScBr_6$	3.76	1.93	10.19 %
Rb_2AuScI_6	4.90	2.20	14.07 %

The static value of reflectivity is less than 15 % (see Table 4) for the explored compounds. The lowest reflectivity R(ω) indicates that both materials are thought to be more effective for incoming light, with energy values ranging from zero to the gap in the band, as shown in Fig. 7 (d). The computed value of L(ω) measures the amount of energy (less than 0.3 in the visible range) that disappears when a photon travels through a substance, as shown in Fig. 7(e). A very low reflectivity and loss function value are significant for the materials to be used as absorbing layers in solar cells.

3.5. Thermoelectric properties

Given the increasing demand for energy, waste heat recovery—a method that transforms heat into electrical energy—becomes increasingly important in systems to improve material efficiency. Thermoelectric (TE) materials produce portable power for distant missions, energy devices, and cooling applications. An analysis of a compound's transport properties is necessary to determine whether it is appropriate for these uses. For the materials under study, effective thermoelectric conversion requires reducing heat conductivity (k) and increasing electrical conductivity (σ). The See-beck coefficient (S), power factor (PF), and figure of merit (ZT) would all rise as a result of this. Additional information, such as a smaller band gap and greater carrier mobility, must be considered when analyzing TE materials.

These materials' electronic band structure and phonons' dispersion—vibrations that move heat across the lattice—determine their thermoelectric (TE) properties. To calculate the TE behaviour with respect to temperature, we employ the Boltzmann transport theory [90]. Specifically, we utilize the Boltztrap2 code [47] for integrating Fermi energy, a process dependent on the concentration of both n and p-type charge carriers. Additionally, we incorporate the electronic components of thermal conductivity (K_e) and electrical conductivity (σ) into the calculation, considering a relaxation time (τ = 10^{-14}s).

Electrical conductivity (σ) measures how well a material conducts electricity, as follows [91]: σ = nqμ, where n represents the concentration of the carrier, q represents the charge of the carrier, and μ represents the mobility of the carrier. The initial electrical conductivity values at 200K for Cs_2AuScX_6 (Rb_2AuScX_6), where X represents Cl, Br, or I, are 0.73 (0.66) × 10^5, 0.56 (0.55) × 10^5, and 0.54 (0.57) × 10^5 (1/Ω.m), respectively. A key feature of semiconductors is that all compounds increase their electrical conductivity with temperature [92]. Moreover, the I-based compound outperforms the Br and Cl-based compounds, achieving the greatest conductivity values as the temperature becomes closer to its maximum range of 200–1000K, as shown in Fig. 8(a). This is explained by the fact that more bonds are broken in halides based on Cs and Rb. At high temperatures (1000K), $Cs_2AuScCl_6$ ($Rb_2AuScCl_6$), $Cs_2AuScBr_6$ ($Rb_2AuScBr_6$), and Cs_2AuScI_6 (Rb_2AuScI_6) exhibit electrical conductivity values of 2.27 (2.29) × 10^5, 2.38 (2.39) × 10^5, and 2.53 (2.58) × 10^5 (1/Ω.m), respectively.

The trends in the graphs of K_e and σ versus temperature (T) are roughly the same. Electronic conductivity increases with temperature. As can be seen in Fig. 8(b), the highest values of 1.58 (1.66), 2.05 (2.15),

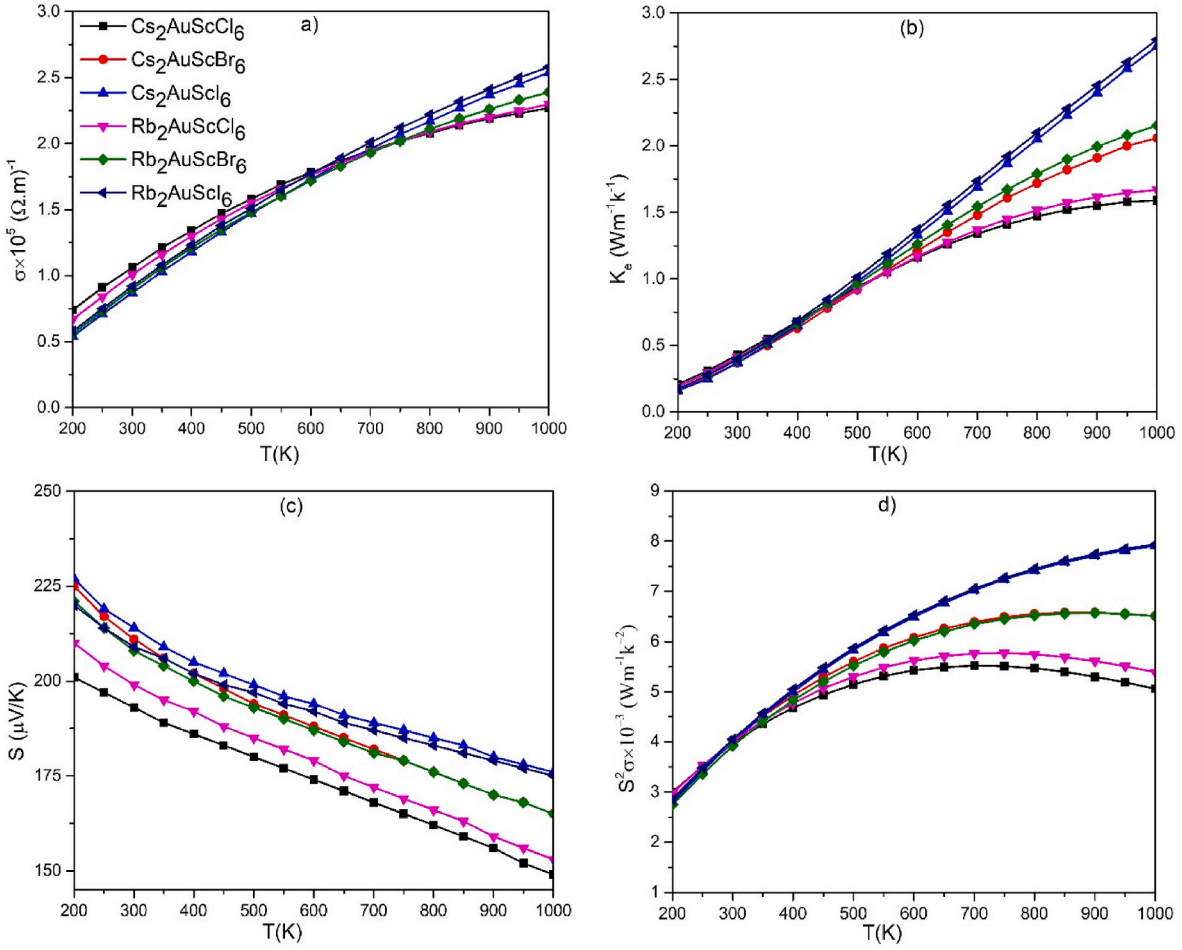

Fig. 8. The computed a) Electrical conductivity, σ, b) Electronic part of thermal conductivity, K_e, c) See-beck coefficient, S, and d) Power factor (PF) $S^2\sigma$ of the studied compounds.

Table 5
Room temperature computed values of electrical conductivity (σ), electronic conductivity (Ke), See-beck coefficient (S), power factor (PF), and figure of merit (ZT) of the investigated compounds by TB-mBJ approach.

Compound	σ × 10^5 (1/Ω.m)	K_e ($Wm^{-1}k^{-1}$)	S (μV/K)	PF × 10^{-3} ($Wm^{-1}k^{-2}$)	ZT*	True ZT
$Cs_2AuScCl_6$	1.06	0.43	193	3.98	0.92	0.44
$Cs_2AuScBr_6$	0.90	0.37	211	4.03	1.07	0.47
Cs_2AuScI_6	0.87	0.37	214	4.01	1.06	0.62
$Rb_2AuScCl_6$	1.01	0.41	199	4.02	0.97	0.47
$Rb_2AuScBr_6$	0.90	0.39	208	3.92	0.99	0.53
Rb_2AuScI_6	0.92	0.39	209	4.06	1.01	0.54

ZT* (without lattice thermal contribution).

and 2.75 (2.79) $Wm^{-1}k^{-1}$ are obtained at 1000K for $Cs_2AuScCl_6$ ($Rb_2AuScCl_6$), $Cs_2AuScBr_6$ ($Rb_2AuScBr_6$), and Cs_2AuScI_6 (Rb_2AuScI_6), respectively. The low thermal conductivity (K), which is the sum of K_L and K_e [93,94] and high σ values of these materials make them appropriate for thermoelectric applications. Table 5 provides the computed parameters for σ and K_e at room temperature (300K). Interestingly, their electrical conductivity (σ) is a factor of 10^5 higher than their electronic conductivity (K_e), highlighting their considerable potential for opto-electronic applications.

When applying a temperature gradient, the See-beck coefficient (S) measures the voltage produced across a material (i.e., $= -\frac{\Delta V}{\Delta T}$). In thermoelectric materials, a high See-beck coefficient is highly desirable [95]. Notably, the See-beck coefficient decreases as the temperature rises. In the case of Cs (Rb)-based compositions containing Cl, Br, and I atoms, the S values decrease from 201 to 149 (210–153) μV/K, 225 to 165 (221–165) μV/K, and 227 to 176 (220–175) μV/K, respectively, over the temperature range of 200–1000K, as displayed in Fig. 8(c). The S values observed at 300K are given in Table 5 and exhibit the following trend: Cs_2AuScI_6>$Cs_2AuScBr_6$>$Cs_2AuScCl_6$ for Cs-based halides and Rb_2AuScI_6 > $Rb_2AuScBr_6$ > $Rb_2AuScCl_6$ for Rb-based halides. Because these compounds have positive S values within the designated temperature range, they are classified as P-type.

One of the most important factors in assessing a material's TE characteristics is its power factor. It measures how well a thermoelectric material transforms heat into electrical power. In mathematics, the power factor is defined as [96]: PF=$S^2\sigma$, where S represents the See-beck coefficient, also known as thermo-power or thermoelectric voltage, and σ denotes the electrical conductivity. The graph illustrating PF versus temperature (T) can be seen in Fig. 8(d). As temperature increases, the power factor also rises, reaching its peak values of 5.51 × 10^{-3} $Wm^{-1}k^{-2}$, 6.55 × 10^{-3} $Wm^{-1}k^{-2}$, and 7.88 × 10^{-3} $Wm^{-1}k^{-2}$ at 700K, 800K, and 1000K for $Cs_2AuScCl_6$, $Cs_2AuScBr_6$, and Cs_2AuScI_6, respectively. For $Rb_2AuScCl_6$, $Rb_2AuScBr_6$, and Rb_2AuScI_6, the corresponding values are 5.76 × 10^{-3} $Wm^{-1}k^{-2}$, 6.54 × 10^{-3} $Wm^{-1}k^{-2}$, and 7.90 × 10^{-3} $Wm^{-1}k^{-2}$ at 700K, 800K, and 1000K, respectively. However, the studied compounds have higher PF at room temperature than some known TE materials, such as 1.95 × 10^{-3} $Wm^{-1}k^{-2}$ and 1.93 × 10^{-3} $Wm^{-1}k^{-2}$ for Tl_2(Se, Te)Cl_6 [97].

The ZT value is a dimensionless figure of merit that assesses the effectiveness of the TE materials in association with the aforementioned

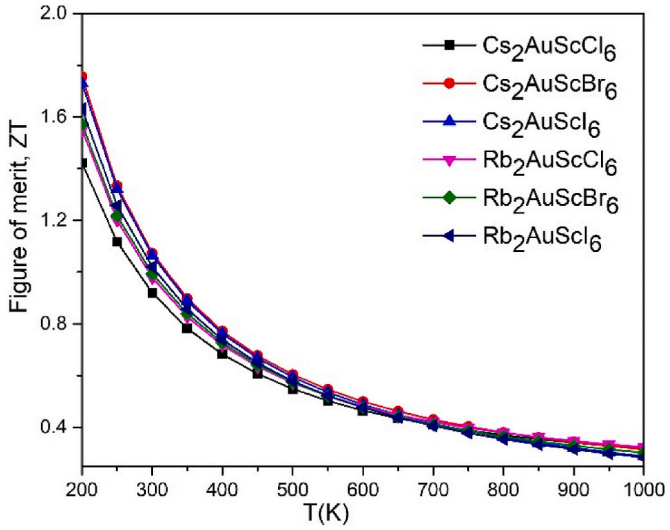

Fig. 9. Figure of merit (ZT) of the studied compounds (without lattice or phonon contribution).

characteristics. The measurement of the dimensionless figure of merit is used to measure thermoelectric material efficiency. *ZT* is defined as [98]: $ZT = \frac{S^2\sigma}{K}T$, where *K* is the thermal conductivity made up of the electronic and lattice parts, σ is the electrical conductivity, and *S* is the thermo-power. Promising TE materials are those with a high ZT~1.0, which may be attained when the power factor $S^2\sigma$ is high and the thermal conductivity is low [99]. Nevertheless, it is important to remember that a rise in temperature causes the *ZT* value to decrease without consideration of the lattice thermal contribution. As a result, the *ZT* values at 300K for compositions based on Cs and including Cl, Br, and I atoms are 0.92, 1.07, and 1.06, respectively, whereas for compositions based on Rb and containing Cl, Br, and I atoms, they are 0.97, 0.99, and 1.01, respectively. These are not true ZT values because Boltztrap2 can not calculate the lattice thermal contribution (K_L), as shown in Fig. 9.

To find the accurate ZT values, the lattice part of thermal contribution (K_L) is considered and calculated by the Glen A. Slack formula [100] in the thermo-mechanical section (supplementary data, Table S1). The effects of K_L in a certain temperature range of 200–1000K are shown in Fig. 10(a). Adding the two contributions (i.e., $K = Ke + K_L$) yields the true efficiency of the material. The ZT values decreased as the lattice or phonon contribution became dominant. The actual values of ZT at 300K are found to be 0.44, 0.47, and 0.62 for $Cs_2AuScCl_6$, $Cs_2AuScBr_6$, and Cs_2AuScI_6, and 0.47, 0.53, and 0.54 for $Rb_2AuScCl_6$, $Rb_2AuScBr_6$, and Rb_2AuScI_6, which are precisely consistent with the Rb_2LiTlX_6 (X = Cl, Br) [101] DP halide compounds. Fig. 10(b) shows the obtained true ZT values. It should be noted that the Glen A. Slack equation overestimates the actual value of the theoretical calculation of K_L by largely [102]. Therefore, a higher ZT value is expected for the compounds that we found using the K_L values obtained via the Glen A. Slack equation. Similar reports are also available in Ref. [97]. Therefore, the studied DP materials could fulfill the necessity for waste heat management and sustainable energy solutions.

4. Conclusions

The ground state structure is obtained for the titled compounds by the DFT calculations with the aid of the Wien2k code. The structural stability is confirmed by the formation energy, binding energy, phonon dispersion curve, stiffness constants, tolerance, and octahedral factors. The lattice parameter increases from 10.5326 (10.4480) Å to 11.0869 (11.0197) Å and 11.8920 (11.8452) Å as the halide (X = Cl, Br, I) ionic radius increases for Cs (Rb)-based compositions. The electronic band structure confirms the semiconducting nature. The TB mBJ potential calculations reveal the energy band gaps are 1.88, 1.68, and 1.30 eV for Cs_2AuScX_6 (X = Cl, Br, I) and 1.93, 1.71, and 1.32 eV for Rb_2AuScX_6 (X = Cl, Br, I), respectively. The band gap values of the DP of the titled compounds are close to the S. Q. limit [62] for maximum efficiency, which makes them suitable for application in solar cell devices. The low effective mass of electrons and holes obtained is favorable for energy technology devices. The DOS and charge density mapping plots explore the bonding nature present within the studied materials. The important optical constants demonstrate the studied material's response to the incident photon. The usefulness of the titled compounds in optoelectronic applications stems from their high absorption coefficients of 10^6 order and other optical constants, including low energy loss and reflection capacity (reflectivity is less than 15 %). The DPs, A_2AuScX_6 (A = Cs, Rb; X = Cl, Br, I), are, therefore, promising options for efficient solar cells and reasonably priced optoelectronic devices. Analysis of thermoelectric properties reveals essential prospects for the titled compounds. The ZT values of 0.44, 0.47, 0.62, 0.47, 0.53, and 0.54 calculated using power factor and thermal conductivity at 300K for $Cs_2AuScCl_6$, $Cs_2AuScBr_6$, Cs_2AuScI_6, $Rb_2AuScCl_6$, $Rb_2AuScBr_6$, and Rb_2AuScI_6, respectively, imply that the studied compounds are promising thermoelectric materials. The elastic properties certify the ductility that confirms the studied compound's machinability, which is essential

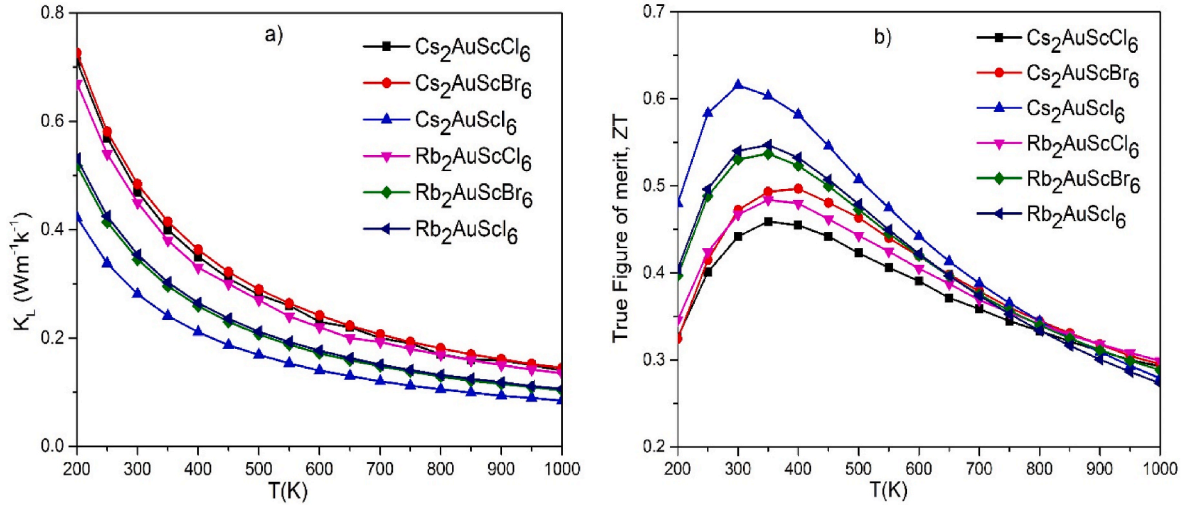

Fig. 10. a) Lattice or phonon thermal conductivity, K_L (derived from supplementary part), and b) True Figure of merit (ZT) of the studied compounds.

for device fabrication. Moreover, high melting points and low K_{min} values also support their high-temperature use. In the end, the obtained results of the titled DPs are encouraging and hope that this study will provide proper guidance for future research on energy harvesting materials.

CRediT authorship contribution statement

S. Mahmud: Writing – original draft, Validation, Methodology, Formal analysis, Data curation, Conceptualization. **M.A. Ali:** Writing – original draft, Validation, Supervision, Project administration, Methodology, Formal analysis, Conceptualization. **M.M. Hossain:** Writing – review & editing, Validation. **M.M. Uddin:** Writing – review & editing, Validation.

Declaration of competing interest

The authors declare that they have no known competing financial interests or personal relationships that could have appeared to influence the work reported in this paper.

Data availability

Data will be made available on request.

Acknowledgments

This work was carried out with the aid of a grant (grant number: 21-378 RG/PHYS/AS_G -FR3240319526) from UNESCO-TWAS and the Swedish International Development Cooperation Agency (SIDA). The views expressed herein do not necessarily represent those of UNESCO-TWAS, SIDA or its Board of Governors.

Appendix A. Supplementary data

Supplementary data to this article can be found online at https://doi.org/10.1016/j.vacuum.2023.112926.

References

[1] W.J. Yin, B. Weng, J. Ge, Q. Sun, Z. Li, Y. Yan, Oxide perovskites, double perovskites and derivatives for electrocatalysis, photocatalysis, and photovoltaics, Energy Environ. Sci. 12 (2) (2019) 442–462.
[2] P.K. Kung, M.H. Li, P.Y. Lin, et al., Lead-free double perovskites for perovskite solar cells, Sol. RRL 4 (2) (2020), 1900306.
[3] S.A. Dar, B. Want, Direct band gap double perovskite halide $Cs_2ScInCl_6$ for optoelectronic applications—a first principle study, Comput Condens Matter 33 (2022), e00736.
[4] A. Kaltzoglou, M. Antoniadou, A.G. Kontos, et al., Optical-vibrational properties of the Cs_2SnX_6 (X= Cl, Br, I) defect perovskites and hole-transport efficiency in dye-sensitized solar cells, J. Phys. Chem. C 120 (22) (2016) 11777–11785.
[5] C.N. Savory, A. Walsh, D.O. Scanlon, Can Pb-free halide double perovskites support high-efficiency solar cells? ACS Energy Lett. 1 (5) (2016) 949–955.
[6] J. Chen, X. Cai, D. Yang, et al., Recent progress in stabilizing hybrid perovskites for solar cell applications, J. Power Sources 355 (2017) 98–133.
[7] B. Lee, C.C. Stoumpos, N. Zhou, et al., Air-stable molecular semiconducting iodosalts for solar cell applications: Cs_2SnI_6 as a hole conductor, J. Am. Chem. Soc. 136 (43) (2014) 15379–15385.
[8] A.E. Maughan, A.M. Ganose, M.M. Bordelon, E.M. Miller, D.O. Scanlon, J. R. Neilson, Defect tolerance to intolerance in the vacancy-ordered double perovskite semiconductors Cs_2SnI_6 and Cs_2TeI_6, J. Am. Chem. Soc. 138 (27) (2016) 8453–8464.
[9] M.J. Fang, C.W. Tsao, Y.J. Hsu, Semiconductor nanoheterostructures for photoconversion applications, J. Phys. D Appl. Phys. 53 (14) (2020), 143001.
[10] M. Kumar, A. Raj, A. Kumar, A. Anshul, Theoretical evidence of high power conversion efficiency in double perovskite solar cell device, Opt. Mater. 111 (2021), 110565.
[11] H. Tang, Y. Xu, X. Hu, et al., Lead-free halide double perovskite Nanocrystals for light-Emitting applications: Strategies for Boosting efficiency and stability, Adv. Sci. 8 (7) (2021), 2004118.
[12] S. Kurtz, I. Repins, W.K. Metzger, et al., Historical analysis of champion photovoltaic module efficiencies, IEEE J. Photovoltaics 8 (2) (2018) 363–372.
[13] S Il Seok, M. Grätzel, N.G. Park, Methodologies toward highly efficient perovskite solar cells, Small 14 (20) (2018), 1704177.
[14] J. Park, J. Kim, H.S. Yun, et al., Controlled growth of perovskite layers with volatile alkylammonium chlorides, Nature 616 (7958) (2023) 724–730.
[15] J. Zhou, J. Huang, Photodetectors based on organic–inorganic hybrid lead halide perovskites, Adv. Sci. 5 (1) (2018), 1700256.
[16] Q. Chen, N. De Marco, Y.M. Yang, et al., Under the spotlight: the organic–inorganic hybrid halide perovskite for optoelectronic applications, Nano Today 10 (3) (2015) 355–396.
[17] X.G. Zhao, D. Yang, J.C. Ren, Y. Sun, Z. Xiao, L. Zhang, Rational design of halide double perovskites for optoelectronic applications, Joule 2 (9) (2018) 1662–1673.
[18] L. Chu, W. Ahmad, W. Liu, et al., Lead-free halide double perovskite materials: a new superstar toward green and stable optoelectronic applications, Nano-Micro Lett. 11 (2019) 1–18.
[19] A. Bibi, I. Lee, Y. Nah, et al., Lead-free halide double perovskites: toward stable and sustainable optoelectronic devices, Mater. Today 49 (2021) 123–144.
[20] B. Cai, X. Chen, M. Xie, et al., A class of Pb-free double perovskite halide semiconductors with intrinsic ferromagnetism, large spin splitting and high Curie temperature, Mater Horizons 5 (5) (2018) 961–968.
[21] S. Khawar, M.Q. Afzal, M. Husain, et al., First-principles calculations to investigate structural, electronic, optical, and magnetic properties of a scintillating double perovskite halide ($Cs_2LiCeCl_6$), J. Mater. Res. Technol. 21 (2022) 4790–4798.
[22] K. Radja, B.L. Farah, A. Ibrahim, et al., Investigation of structural, magneto-electronic, elastic, mechanical and thermoelectric properties of novel lead-free halide double perovskite $Cs_2AgFeCl_6$: first-principles calcuations, J Phys Chem Solids 167 (2022), 110795.
[23] X. Xu, Y. Zhong, Z. Shao, Double perovskites in catalysis, electrocatalysis, and photo (electro) catalysis, Trends Chem 1 (4) (2019) 410–424.
[24] Z. Zhang, Y. Liang, H. Huang, et al., Stable and highly efficient photocatalysis with lead-free double-perovskite of $Cs_2AgBiBr_6$, Angew Chemie Int Ed 58 (22) (2019) 7263–7267.
[25] R. Hu, R. Ding, J. Chen, J. Hu, Y. Zhang, Preparation and catalytic activities of the novel double perovskite-type oxide La_2CuNiO_6 for methane combustion, Catal. Commun. 21 (2012) 38–41.
[26] A.J. Kale, R. Chaurasiya, A. Dixit, Lead-free $Cs_2BB'X_6$ (B: Ag/Au/Cu, B′: Bi/Sb/Tl, and X: Br/Cl/I) double perovskites and their potential in energy conversion applications, ACS Appl. Energy Mater. 5 (9) (2022) 10427–10445.
[27] N.A. Noor, M.W. Iqbal, T. Zelai, et al., Analysis of direct band gap A_2ScInI_6 (A= Rb, Cs) double perovskite halides using DFT approach for renewable energy devices, J. Mater. Res. Technol. 13 (2021) 2491–2500.
[28] F. Aslam, H. Ullah, M. Hassan, Theoretical investigation of Cs_2InBiX_6 (X= Cl, Br, I) double perovskite halides using first-principle calculations, Mater. Sci. Eng. B 274 (2021), 115456.
[29] K.I. Kobayashi, T. Kimura, H. Sawada, K. Terakura, Y. Tokura, Room-temperature magnetoresistance in an oxide material with an ordered double-perovskite structure, Nature 395 (6703) (1998) 677–680.
[30] S. Yáñez-Vilar, E.D. Mun, V.S. Zapf, et al., Multiferroic behavior in the double-perovskite Lu_2MnCoO_6, Phys. Rev. B 84 (13) (2011), 134427.
[31] B.C. Jeon, C.H. Kim, S.J. Moon, et al., Electronic structure of double perovskite A_2FeReO_6 (A= Ba and Ca): interplay between spin–orbit interaction, electron correlation, and lattice distortion, J. Phys. Condens. Matter 22 (34) (2010), 345602.
[32] A.H. Slavney, T. Hu, A.M. Lindenberg, H.I. Karunadasa, A bismuth-halide double perovskite with long carrier recombination lifetime for photovoltaic applications, J. Am. Chem. Soc. 138 (7) (2016) 2138–2141.
[33] M. Tariq, M.A. Ali, A. Laref, G. Murtaza, Anion replacement effect on the physical properties of metal halide double perovskites Cs_2AgInX_6 (X= F, Cl, Br, I), Solid State Commun. 314 (2020), 113929.
[34] E.T. McClure, M.R. Ball, W. Windl, P.M. Woodward, Cs_2AgBiX_6 (X = Br, Cl): new visible light absorbing, lead-free halide perovskite semiconductors, Chem. Mater. 28 (5) (2016) 1348–1354, https://doi.org/10.1021/acs.chemmater.5b04231.
[35] F. Igbari, R. Wang, Z.K. Wang, et al., Composition stoichiometry of $Cs_2AgBiBr_6$ films for highly efficient lead-free perovskite solar cells, Nano Lett. 19 (3) (2019) 2066–2073.
[36] G. Volonakis, A.A. Haghighirad, R.L. Milot, et al., $Cs_2InAgCl_6$: a new lead-free halide double perovskite with direct band gap, J. Phys. Chem. Lett. 8 (4) (2017) 772–778.
[37] S.A. Dar, B. Want, DFT study of structural, mechanical, and opto-electronic properties of scadium-based halide double perovskite $Cs_2ScInBr_6$ for optoelectronic applications, Micro and Nanostructures 170 (2022), 207370.
[38] N. Erum, J. Ahmad, M.A. Iqbal, M. Ramzan, DFT insights of mechanical, optoelectronic and thermoelectric properties for Cs_2ScTlX_6 (X = Cl, Br, I) double perovskites, Opt Quantum Electron 55 (4) (2023) 1–15, https://doi.org/10.1007/s11082-022-04538-2.
[39] Y. Sun, A.J. Fernández-Carrión, Y. Liu, et al., Bismuth-based halide double perovskite $Cs_2LiBiCl_6$: crystal structure, luminescence, and stability, Chem. Mater. 33 (15) (2021) 5905–5916, https://doi.org/10.1021/acs.chemmater.1c00854.
[40] P. Liu, Y. Sun, A.J. Fernández-Carrión, et al., Bismuth-based halide double perovskite Cs_2KBiCl_6: Disorder and luminescence, Chinese Chem Lett (2023), 108641, https://doi.org/10.1016/j.cclet.2023.108641. Published online.
[41] M.G.B. Ashiq, H. Albalawi, Study of electronic, mechanical, thermoelectric and optical properties of K_2ScAuZ_6 (Z= Br, I) for energy harvesting, Eur Phys J Plus 138 (6) (2023) 1–12.
[42] P. Blaha, K. Schwarz, G.K.H. Madsen, D. Kvasnicka, J. Luitz, others. wien2k, An Augment Pl wave+ local orbitals Progr Calc Cryst Prop 60 (2001) 1–302.

[43] J.P. Perdew, K. Burke, M. Ernzerhof, Generalized gradient approximation made simple, Phys. Rev. Lett. 77 (18) (1996) 3865.

[44] E. Wimmer, H. Krakauer, M. Weinert, A.J. Freeman, Full-potential self-consistent linearized-augmented-plane-wave method for calculating the electronic structure of molecules and surfaces: O_2 molecule, Phys. Rev. B 24 (2) (1981) 864.

[45] M. Jamal, M. Bilal, I. Ahmad, S. Jalali-Asadabadi, IRelast package, J. Alloys Compd. 735 (2018) 569–579.

[46] F. Tran, P. Blaha, Accurate band gaps of semiconductors and insulators with a semilocal exchange-correlation potential, Phys. Rev. Lett. 102 (22) (2009), 226401.

[47] G.K.H. Madsen, J. Carrete, M.J. Verstraete, BoltzTraP2, a program for interpolating band structures and calculating semi-classical transport coefficients, Comput. Phys. Commun. 231 (2018) 140–145, https://doi.org/10.1016/j.cpc.2018.05.010.

[48] V.M. Goldschmidt, Die gesetze der krystallochemie, Naturwissenschaften 14 (21) (1926) 477–485.

[49] R.D. Shannon, Revised effective ionic radii and systematic studies of interatomic distances in halides and chalcogenides, Acta Crystallogr Sect A Cryst physics, diffraction, Theor Gen Crystallogr. 32 (5) (1976) 751–767.

[50] S.A. Mir, D.C. Gupta, Analysis of cage structured halide double perovskites Cs_2NaMCl_6 (M= Ti, V) by spin polarized calculations, J. Alloys Compd. 854 (2021), 156000.

[51] X. Du, D. He, H. Mei, Y. Zhong, N. Cheng, Insights on electronic structures, elastic features and optical properties of mixed-valence double perovskites $Cs_2Au_2X_6$ (X= F, Cl, Br, I), Phys. Lett. 384 (8) (2020), 126169.

[52] J.S. Ghotra, M.B. Hursthouse, A.J. Welch, J.C. Soc, D. Trans, Inorg. Chem. 17 (8) (1978) 2319–2320. Vol. 17, No. 8, 1978 2319.

[53] M. Roy, S. Ghorui, A. Alam, M. Aslam, others, Facile strategy to synthesize cesium gold-based bromide perovskites: an integrated experimental and theoretical approach to study temperature-dependent structural and optical properties, J. Mater. Chem. C 10 (11) (2022) 4224–4235.

[54] S. Wang, S. Hirai, M.C. Shapiro, et al., Pressure-induced symmetry breaking in tetragonal $CsAuI_3$, Phys Rev B - Condens Matter Mater Phys. 87 (5) (2013) 1–6, https://doi.org/10.1103/PhysRevB.87.054104.

[55] A. Jain, S.P. Ong, G. Hautier, et al., Commentary: the materials project: a materials genome approach to accelerating materials innovation, Apl. Mater. 1 (1) (2013), https://doi.org/10.1063/1.4812323.

[56] D.I. Bolef, M. Menes, Measurement of elastic constants of RbBr, RbI, CsBr, and CsI by an ultrasonic cw resonance technique, J. Appl. Phys. 31 (6) (1960) 1010–1017, https://doi.org/10.1063/1.1735736.

[57] S. Kirklin, J.E. Saal, B. Meredig, et al., The open Quantum materials Database (OQMD): assessing the accuracy of DFT formation energies, npj Comput. Mater. 1 (October) (2015), https://doi.org/10.1038/npjcompumats.2015.10.

[58] G. Meyer, J.D. Corbett, Reduced ternary halides of scandium: $RbScX_3$ (X= chlorine, bromine) and $CsScX_3$ (X= chlorine, bromine, iodine), Inorg. Chem. 20 (8) (1981) 2627–2631.

[59] T. Katsura, Y. Tange, A simple derivation of the Birch–Murnaghan equations of state (EOSs) and comparison with EOSs derived from other definitions of finite strain, Minerals 9 (12) (2019) 745.

[60] M. Markov, X. Hu, H.C. Liu, et al., Semi-metals as potential thermoelectric materials, Sci. Rep. 8 (1) (2018) 9876.

[61] F. Tran, P. Blaha, K. Schwarz, Band gap calculations with Becke-Johnson exchange potential, J. Phys. Condens. Matter 19 (19) (2007), https://doi.org/10.1088/0953-8984/19/19/196208.

[62] B. Ehrler, E. Alarcón-Lladó, S.W. Tabernig, T. Veeken, E.C. Garnett, A. Polman, Photovoltaics reaching for the shockley-queisser limit, ACS Energy Lett. 5 (9) (2020) 3029–3033, https://doi.org/10.1021/acsenergylett.0c01790.

[63] Y. Xu, T. Gong, J.N. Munday, The generalized Shockley-Queisser limit for nanostructured solar cells, Sci. Rep. 5 (2015) 1–9, https://doi.org/10.1038/srep13536.

[64] W. Shockley, H.J. Queisser, Detailed balance limit of efficiency of p-n junction solar cells, J. Appl. Phys. 32 (3) (1961) 510–519, https://doi.org/10.1063/1.1736034.

[65] T. Sun, Z. Ma, M. Yao, J. Wei, Y. Liu, X. Ming, Direct band-gap iodide double perovskite solar cell materials by doping strategy: first-principles predictions, Mater. Today Commun. 37 (August) (2023), 107055, https://doi.org/10.1016/j.mtcomm.2023.107055.

[66] T. Nakajima, K. Sawada, Discovery of Pb-free perovskite solar cells via high-throughput simulation on the K computer, J. Phys. Chem. Lett. 8 (19) (2017) 4826–4831.

[67] T. Saha, M.M.H. Babu, M. Arifuzzaman, J. Podder, Thermodynamic and dynamic stability in a new potential $Cs_2AgAsCl_6$ perovskite: insight from DFT study, Phys. Chem. Chem. Phys. 24 (43) (2022) 26609–26621.

[68] X. Zhang, J.X. Shen, W. Wang, C.G. de Walle, First-principles analysis of radiative recombination in lead-halide perovskites, ACS Energy Lett. 3 (10) (2018) 2329–2334.

[69] B. Wu, Y. Zhou, G. Xing, et al., Long minority-carrier diffusion length and low surface-recombination velocity in inorganic lead-free $CsSnI_3$ perovskite crystal for solar cells, Adv. Funct. Mater. 27 (7) (2017), 1604818.

[70] W. Gao, C. Ran, J. Xi, et al., High-quality $Cs_2AgBiBr_6$ double perovskite film for lead-free inverted planar heterojunction solar cells with 2.2% efficiency, ChemPhysChem 19 (14) (2018) 1696–1700.

[71] M.S. Shadabroo, H. Abdizadeh, M.R. Golobostanfard, Elpasolite structures based on A_2AgBiX_6 (A: MA, Cs, X: I, Br): application in double perovskite solar cells, Mater. Sci. Semicond. Process. 125 (2021), 105639.

[72] M. Wang, P. Zeng, S. Bai, et al., High-quality sequential-vapor-deposited $Cs_2AgBiBr_6$ thin films for lead-free perovskite solar cells, Sol. RRL 2 (12) (2018), 1800217.

[73] S. Das, M. Debbarma, S. Chattopadhyaya, Calculations of physical properties of Ba_2GdSbO_6 (BGSO) double perovskite for thermoelectric and solar cell applications, Phys. B Condens. Matter 664 (2023), 414979.

[74] R. Sa, Y. Wei, W. Zha, D. Liu, A first-principle study of the structural, mechanical, electronic and optical properties of vacancy-ordered double perovskite Cs_2TeX_6 (X= Cl, Br, I), Chem. Phys. Lett. 754 (2020), 137538.

[75] M. Wuttig, C.F. Schön, M. Schumacher, et al., Halide perovskites: advanced photovoltaic materials empowered by a unique bonding mechanism, Adv. Funct. Mater. 32 (2) (2022), 2110166.

[76] M. Fox, Optical Properties of Solids, 2002. Published online.

[77] A. Kojima, K. Teshima, Y. Shirai, T. Miyasaka, Organometal halide perovskites as visible-light sensitizers for photovoltaic cells, J. Am. Chem. Soc. 131 (17) (2009) 6050–6051.

[78] R.D. Grimes, E.R. Cowley, A model dielectric function for semiconductors, Can. J. Phys. 53 (23) (1975) 2549–2554.

[79] D.Y. Hu, X.H. Zhao, T.Y. Tang, et al., First-principles study on the structural, elastic, electronic and optical properties of lead-free double perovskites Cs_2CuBiX_6 (XI, Br, Cl), Mater. Today Commun. 29 (2021), 102842.

[80] D.Y. Hu, X.H. Zhao, T.Y. Tang, L. Li, Y.L. Tang, Insights on structural, elastic, electronic and optical properties of double-perovskite halides Rb_2CuBiX_6 (X= Br, Cl), J Phys Chem Solids 167 (2022), 110791.

[81] D.Y. Hu, X.H. Zhao, T.Y. Tang, et al., Revealing structural, elastic, electronic and optical properties of potential perovskites K_2CuBiX_6 (X= Br, Cl) based on first-principles, J. Solid State Chem. 310 (2022), 123046.

[82] Y. Liu, Y. Huang, Z. Yang, et al., Hexagonal lead-free Cs_2AgBiI_6 perovskite Nanocrystals: a promising material for solar cell application, ACS Appl. Energy Mater. (2023). Published online.

[83] M. Houari, B. Bouadjemi, A. Abbad, T. Lantri, S. Haid, Lead-free Semiconductors with High Absorption : Insight into the Optical Properties of $K_2GeSnBr_6$ and K_2GeSnI_6 Halide Double Perovskites, vol. 112, 2020, pp. 364–369, https://doi.org/10.1134/S0021364020180010, 6.

[84] Q. Mahmood, M. Hassan, S.H.A. Ahmad, A. Shahid, A. Laref, Journal of Physics and Chemistry of Solids Study of optoelectronic and thermoelectric properties of $BaSiO_3$ perovskite under moderate pressure for energy renewable devices applications, J Phys Chem Solids 120 (February) (2018) 87–95, https://doi.org/10.1016/j.jpcs.2018.04.024.

[85] N. Dhar, A. Bandyopadhyay, D. Jana, Tuning electronic, magnetic and optical properties of germanene nanosheet with site dependent adatoms arsenic and gallium: a first principles study, Curr. Appl. Phys. 17 (4) (2017) 573–583.

[86] P. Sharma, S.C. Katyal, Determination of optical parameters of a-$(As_2Se_3)_{90}Ge_{10}$ thin film, J. Phys. D Appl. Phys. 40 (7) (2007) 2115–2120, https://doi.org/10.1088/0022-3727/40/7/038.

[87] C. Li, X. Lu, W. Ding, L. Feng, Y. Gao, Z. Guo, Formability of abx_3 (x = f, cl, br,i) halide perovskites, Acta Crystallogr. Sect. B Struct. Sci. 64 (6) (2008) 702–707.

[88] H.H. Hegazy, G.M. Mustafa, A. Nawaz, N.A. Noor, A. Dahshan, I. Boukhris, Tuning of direct bandgap of Rb_2ScTlX_6(X = Cl, Br, I) double perovskites through halide ion substitution for solar cell devices, J. Mater. Res. Technol. 19 (2022) 1271–1281, https://doi.org/10.1016/j.jmrt.2022.05.082.

[89] C.W. Chen, S.Y. Hsiao, C.Y. Chen, H.W. Kang, Z.Y. Huang, H.W. Lin, Optical properties of organometal halide perovskite thin films and general device structure design rules for perovskite single and tandem solar cells, J. Mater. Chem. A 3 (17) (2015) 9152–9159.

[90] S. Harris, An Introduction to the Theory of the Boltzmann Equation, Courier Corporation, 2004.

[91] S.R. Hui, P. De Luna, How increasing proton and electron conduction benefits electrocatalytic CO_2 reduction, Matter 4 (5) (2021) 1555–1577, https://doi.org/10.1016/j.matt.2021.02.021.

[92] S. Das, M. Debbarma, D. Ghosh, et al., First-principles calculations to investigate structural, mechanical, electronic, magnetic and thermoelectric properties of Ba_2CaMO_6 (M= Re, Os) cubic double perovskites, Phys. B Condens. Matter 626 (2022), 413554.

[93] M. Sajjad, Q. Mahmood, N. Singh, J.A. Larsson, Ultralow lattice thermal conductivity in double perovskite Cs_2PtI_6: a promising thermoelectric material, ACS Appl. Energy Mater. 3 (11) (2020) 11293–11299.

[94] A.H. Reshak, S.A. Khan, S. Auluck, Thermoelectric properties of a single graphene sheet and its derivatives, J. Mater. Chem. C 2 (13) (2014) 2346–2352.

[95] A. Kumar, S. Bano, B. Govind, A. Bhardwaj, K. Bhatt, D.K. Misra, A review on fundamentals, design and optimization to high ZT of thermoelectric materials for application to thermoelectric technology, J. Electron. Mater. 50 (2021) 6037–6059.

[96] Q. Mahmood, M. Hassan, T.H. Flemban, et al., Optoelectronic and thermoelectric properties of double perovskite Rb_2PtX_6 (X = Cl, Br) for energy harvesting: first-principles investigations, J Phys Chem Solids 148 (2021), 109665, https://doi.org/10.1016/j.jpcs.2020.109665.

[97] M.A. Ali, S.A. Dar, A.A. AlObaid, et al., Appealing perspectives of structural, electronic, mechanical, and thermoelectric properties of Tl_2(Se, Te)Cl_6 vacancy-ordered double perovskites, J Phys Chem Solids 159 (2021), 110258.

[98] J.S. Khan, R. Akram, K. Shahid, S. Rafique, M. Hussain, A. ur Rehman, High electrical conductivity and low thermal conductivity in Bi_2Te_3 mixed PPy/PVP composite nanofibers by electrospinning, Mater. Lett. 351 (2023), 134989, https://doi.org/10.1016/j.matlet.2023.134989.

[99] H. Liu, X. Shi, F. Xu, et al., Copper ion liquid-like thermoelectrics, Nat. Mater. 11 (5) (2012) 422–425.

[100] G.A. Slack, The thermal conductivity of nonmetallic crystals, Solid state Phys 34 (1979) 1–71.
[101] M. Manzoor, M.W. Iqbal, M. Imran, et al., Probing direct bandgap of double perovskites Rb_2LiTlX_6(X = Cl, Br) and optoelectronic characteristics for Solar cell applications: DFT calculations, J. Mater. Res. Technol. 18 (2022) 4775–4785, https://doi.org/10.1016/j.jmrt.2022.04.073.
[102] A.J. Hong, C.L. Yuan, J.M. Liu, Quaternary compounds Ag_2XYSe_4 (X= Ba, Sr; Y= Sn, Ge) as novel potential thermoelectric materials, J. Phys. D Appl. Phys. 53 (11) (2020), 115302.